doi:10.26443/seismica.v2i2.953

The July–December 2022 earthquake sequence in the southeastern Fars Arc of Zagros mountains, Iran

Malte Metz * [1,2], **Behnam Maleki Asayesh** [1,2], **Mohammad Mohseni Aref** [2], **Mohammadreza Jamalreyhani** [3], **Pınar Büyükakpınar** [1,2], **Torsten Dahm** [1,2]

[1]GFZ German Research Centre for Geosciences, Potsdam, Germany, [2]Institute of Geosciences, University of Potsdam, Potsdam, Germany, [3]Institute of Geophysics, University of Tehran, Tehran, Iran

Author contributions: *Conceptualization*: Malte Metz, Behnam Maleki Asayesh, Mohammad Mohseni Aref, Mohammadreza Jamalreyhani. *Methodology*: Malte Metz. *Software*: Malte Metz. *Formal analysis*: Malte Metz, Pınar Büyükakpınar. *Data curation*: Mohammad Mohseni Aref, Mohammadreza Jamalreyhani, Pınar Büyükakpınar. *Writing - original draft*: Malte Metz, Behnam Maleki Asayesh, Mohammad Mohseni Aref, Mohammadreza Jamalreyhani. *Writing - review & editing*: Malte Metz, Behnam Maleki Asayesh, Mohammadreza Jamalreyhani, Pınar Büyükakpınar, Torsten Dahm. *Visualization*: Malte Metz, Behnam Maleki Asayesh, Pınar Büyükakpınar. *Supervision*: Pınar Büyükakpınar, Torsten Dahm.

Abstract Within two hours on 01 July 2022, three earthquakes of M_w 5.8–6.0 hit the SE Fars Arc, Iran. In the following months, the region, characterized by the collision of the Iranian and the Arabian plate, thrust faulting, and salt diapirism, was stroke by more than 120 aftershocks of mL 3.1–5.2, of which two of the largest events occurred within one minute on 23 July 2022 in spatial vicinity to each other. We analyzed both the large mainshocks and aftershocks using different techniques, such as the inversion of seismic and satellite deformation data in a joint process, and aftershock relocation. Our results indicate the activation of thrust faults within the lower sedimentary cover of the region along with high aftershock activity at significantly larger depths, supporting the model of a crustal strain decoupling during the collision in the Fars Arc. We resolved a magnitude difference of > 0.2 magnitude units between seismic and joint seismic and satellite deformation inversions probably caused by afterslip, thereby allowing to bridge between results from international agencies and earlier studies. We also find evidence for an event doublet and triplet activating the same or adjacent faults within the sedimentary cover and the basement.

Non-technical summary On 01 July 2022, three moderate earthquakes with magnitudes of 5.8–6.0 occurred in the Zagros mountain range in the Hormozghan province, SE Iran. Their close occurrence in space and time impedes the analysis of such events. Using seismic and satellite deformation data with well-proven and newly developed earthquake parameter estimation tools, we found evidence for south-dipping thrust events within the shallow sedimentary layer. The relocation of more than 120 aftershocks with local magnitudes 3.1–5.2 revealed a strong spatial concentration in larger depths of 10–15 km beneath the mainshocks. This result is consistent with the scenario of shallow-depth mainshocks followed by separated, deeper aftershock sequences, as already observed at the western edge of the Hormuz Strait.

Production Editor: Gareth Funning
Handling Editor: Wenbin Xu
Copy & Layout Editor: Abhineet Gupta

Signed reviewer(s): Ezgi Karasozen, Wasja Bloch

Received: May 2, 2023
Accepted: August 31, 2023
Published: October 18, 2023

1 Introduction

The north-south convergence of ~2–3 cm yr^{-1} between the Arabian and Eurasian plates has led to active faulting and folding, volcanic activities, mountainous terrain, and variable crustal thickness in the Iranian Plateau (IP) (e.g., Stoecklin, 1968; Vernant et al., 2004). This convergence gave rise to the 1800 km long and 200–300 km wide Zagros continental collision zone in the southwestern part of the IP, which accommodates approximately one-third to one-half of the plate motion (e.g., Vernant et al., 2004; Masson et al., 2005). The Zagros mountain range, which is one of the seismically most active regions in the Alpine-Himalayan orogenic belt, is subdivided into three major tectonostratigraphic domains from SW to NE: (1) the Mesopotamia-Persian Gulf Foreland Basin, (2) the Zagros Fold-Thrust Belt (ZFTB), and (3) High Zagros Zone (HZZ). The Simply Folded Belt (SFB) or Zagros Foreland Folded Belt (ZFFB) as a subdomain of ZFTB, is the topographically lower-elevation part of the range where most of the active deformation in the Zagros is concentrated (e.g., Falcon, 1974; Hessami et al., 2001; Talebian and Jackson, 2004; Alavi, 2007; Oveisi et al., 2009). The SFB itself is laterally subdivided into four physiographic provinces from NW to SE, namely the Kirkuk Embayment, the Lurestan Arc, the Dezful Embayment, and the Fars Arc (FA, see Fig. 1a) (e.g., Stoecklin, 1968; Alavi, 2007; Nissen et al., 2011; Jamalreyhani et al., 2023). The collision zone in the foreland involves 10–15 km thick sections of sedimentary rocks, including extended layers of evaporites

*Corresponding author: mmetz@gfz-potsdam.de

and salt decoupling the deformation in the sedimentary strata from the Arabian continental basement (e.g., Stoecklin, 1968; Jamalreyhani et al., 2023). This exceptional setting has resulted in one of the world's most productive oil and gas basins (Jamalreyhani et al., 2021).

Earthquake multiples and doublets are loosely defined as two (doublet) or more (multiple) triggered and sub-sequential mainshocks of comparable size rupturing the same or adjacent faults within a short time (e.g., Lay and Kanamori, 1980; Ammon et al., 2008). The occurrence of doublets is explained by heterogeneous stress on pre-existing faults with geometrical complexities (e.g., steps, bends) and stress transfers from the first to the second event of the doublet (e.g., Xu and Schwartz, 1993; Jia et al., 2020; Zhang et al., 2021; Taymaz et al., 2022; Astiz et al., 1988). Doublets have been observed in different tectonic settings, as (1) within subduction zones (Lay and Kanamori, 1980; Xu and Schwartz, 1993; Ammon et al., 2008; Lay, 2015; Ye et al., 2013, 2016; Jia et al., 2020), (2) in collision zones (e.g., Thapa et al., 2018), (3) strike-slip fault systems (e.g., Zhang et al., 2021; Sokos et al., 2015; Dal Zilio and Ampuero, 2023), or (4) on normal faults in sedimentary basins (e.g., Cesca et al., 2013).

The central IP and its bounding tectonic structure were hit by several doublets or multiple earthquakes during the last decade, like the NW Iranian 2012 Ahar-Varzagan and 2020 Qotur-Ravian doublets (Ansari, 2016; Ghods et al., 2015; Donner et al., 2015; Momeni and Tatar, 2018; Taymaz et al., 2022), or the December 2017 Hojedk triplet in SE Iran (e.g., Freund, 1970; Walker and Jackson, 2002; Savidge et al., 2019; Asayesh et al., 2020) (Fig. 1a). The occurrence of doublets in the ZFTB is associated with the complex thrust and fold belts in the Zagros mountains with a highly deformed and sliding sedimentary and evaporitic cover with massive syncline and anticline structures (Roustaei et al., 2010). More recently, the ZFTB hosted doublets in Southern Iran, the so-called 2021 Fin doublet (Fathian et al., 2022; Rezapour and Jamalreyhani, 2022), and the 2022 Charak events. These events drew the attention of scientists to the region to better understand the physical mechanism of earthquake doublets, which is crucial for hazard and risk assessment.

Our study area is located in the FA, which is the $\sim$700 km-long segment situated in the East of the SFB with a high-rate seismicity zone in Zagros (Fig. 1b) (e.g., Karasözen et al., 2019). The FA is bounded by the Kazerun Fault in the West and the Bandar Abbas syntaxis in the East and works as the transition zone to the Makran accretionary to the East (Edey et al., 2020) (Fig. 1b). The seismicity of the FA is dominated by shallow thrust events on steeply dipping (30°–60°) blind faults in the sedimentary cover or the underlying crystalline basement (e.g., Jahani et al., 2009; Nissen et al., 2011). Tatar et al. (2004) revealed 10 mm yr^{-1} present-day shortening trending NNE-SSW at the center of the FA. There, surface shortening is accommodated by several W-E to NW-SE trending, symmetric anticlines and synclines with amplitudes within the scale of kilometers and wavelengths of $\sim$10–20 km (e.g., Edey et al., 2020). The relationship between buried seismic faults and surface anticlines in the FA is still debated (Walker et al., 2005). Several surface diapirs, which indicate the presence of the Precambrian-Cambrian Hormuz salt layer between the basement and sedimentary cover, are also observed in the FA (Jahani et al., 2009). The occurrence of anthropogenic earthquakes has recently been reported in this collision zone (Jamalreyhani et al., 2021, and references therein).

On 14 November 2021, the Fin area in the FA was struck by an earthquake doublet (M_w 6.2 and M_w 6.3) (Nemati, 2022; Fathian et al., 2022; Rezapour and Jamalreyhani, 2022) co-located with an earlier sequence of earthquakes (M_w 4.9–5.7) on 25 March 2006 (Roustaei et al., 2010) (Figs. 1c, 2). Furthermore, our study area experienced many significant single events in 2021, including the 16 March NW Lenge earthquake (M_w 5.9), the 15 June Charak earthquake (M_w 5.5), the 21 June Mogham earthquake (M_w 5.2), and the second Charak earthquake on 25 June (M_w 5.6). Some other events, such as the 2005 Qeshm and the 2006 Fin earthquakes, ruptured the lower sedimentary cover and were accompanied by aftershocks in significantly greater depth (Nissen et al., 2010, 2011, 2014). This vertical separation of main- and aftershocks might be driven by the mainshock, causing stress changes within the deeper and harder Hormuz layer. As a result of the stress perturbation, the Hormuz salt may flow, leading to a breakup of intercalated, harder, non-evaporitic sediments and surrounding rocks (Nissen et al., 2014).

Within this tectonic frame, three earthquake sequences with event magnitudes of M_w 5.3–6.1 and a series of aftershocks stroke the Hormozgan Province. The sequences occurred on 01 July 2022 (three earthquakes of M_w 5.7–6.1), further sequence A, on 23 July 2022 (two earthquakes of M_w 5.3–5.6), further sequence B, and on 30 November 2022 (one earthquake of M_w 5.6), further sequence C (Figs. 1c and 2, Tab. 1). All sequences hit the same region SW from the Fin doublet, W from the 2005–2009 seismic sequence on the Island of Qeshm and close to the mapped Zagros Foredeep Fault (ZFF) and Mountain Front Fault (MFF). Different agencies reported the fault mechanisms for these earthquakes, which mainly indicate pure thrust faulting with ENE-WSW to ESE-WNW striking, and N-S oriented shortening. Reported locations scatter primarily along the eastern termination of the ZFF. The only exception is earthquake B2 located $\sim$25 km to the N along the MFF with a strong oblique component. Using satellite geodesy Yang et al. (2023) suggests that two south-dipping, ESE striking thrust faults were activated during the mainshocks A1 and A3 with dip angles of 65° and 33°, a peak slip of $\sim$1.1 m and $\sim$1.3 m, and a geodetic moment release equivalent to M_w 6.22 and M_w 6.23, respectively. Both, A2 and A3, and B1 and B2 occurred in quick succession with interevent times of 60–80 s.

Analysis of earthquake doublets or sequences is challenging, especially when interevent times are smaller than the travel time of surface waves to a station. Then, time windows and stations need to be selected carefully to avoid any overlay of seismic signals (e.g., Jia et al., 2022; Metz et al., 2022). The joint inversion of multiple sources using seismograms and near-field data,

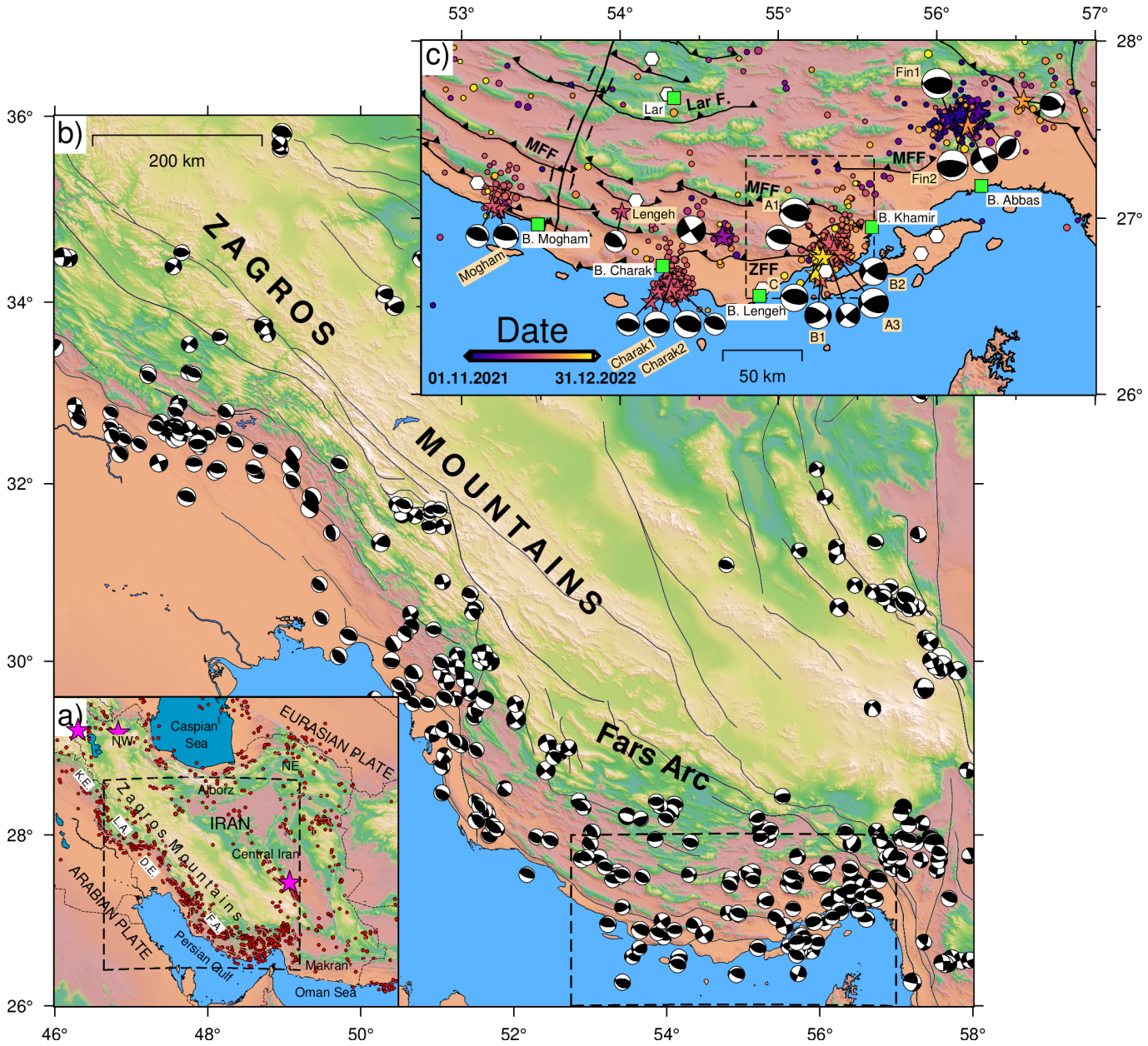

Figure 1 a) The Iranian plateau and its seismotectonic settings. Red circles are $M > 5$ earthquakes from 1900 to 2022 from the USGS catalog. The magenta stars show the location of the 2012 Ahar-Varzagan doublet, the 2020 Qotur-Ravian doublet, and the 2017 Hojedk triplet. The Fars Arc (FA), Dezful embayment (DE), Lurestan Arc (LA), and the Kirkuk embayment (KE) from SE to NW are four tectonostratigraphic domains of the most active part of the Zagros (the Simply Folded Belt). b) SE part of the Zagros Mountains at the leading edge of the Arabia-Eurasia collision zone and focal mechanism of moderate and large events ($M_w \geq 5$) from the gCMT catalog until October 2021. Black lines show major mapped active faults. c) A zoom-in of the Hormozghan area. The white hexagons show the historical events (Ambraseys and Melville, 2005) and colored circles demonstrate the seismicity from November 2021 until December 2022 from the Iranian Seismological Center (IRSC) catalog. Colored stars depict 33 events with $M > 4.5$ during this period. For 20 of them, gCMT reported focal mechanisms (black beach balls). The dashed rectangle depicts the location of Fig. 2.

e.g., static displacements derived from InSAR (Steinberg et al., 2020, 2022), can help to constrain the geometry of and the dislocation on the activated faults within a sequence. Inversions of the rupture kinematics on a doublet fault network can resolve the onset and propagation of the ruptures (e.g., Metz et al., 2022). The back projection of the radiated high-frequency energy helps to unravel the rupture processes (e.g., Daout et al., 2020; Steinberg et al., 2022; Metz et al., 2022). Furthermore, the analysis of aftershocks might help to detect the faults activated during a sequence or doublet (e.g., Ammon et al., 2008; Ghods et al., 2015; Donner et al., 2015; He et al., 2018; Metz et al., 2022).

In this regard, we analyze the July–December 2022 earthquake sequence. We want to clarify if sequence A or B can be classified as an earthquake doublet (or triplet) according to the definition given in the introduction. In this context, we test a newly developed triplet inversion scheme using a combination of satellite deformation with seismic data covering epicentral distances

Table 1 Selected standard centroid moment tensor inversion results published by different agencies for 01 July 2022, 23 July 2022 and 30 November 2022 earthquakes. Centroid times are given.

ID	Agency	Time	Lat, Lon	Depth	M_w	Strike, Dip, Rake
Sequence A: 01 July 2022						
A1	gCMT	21:32:08	26.68°, 55.18°	12 km	6.1	113°, 52°, 110° 282°, 42°, 66°
	GEOFON	21:32:08	26.89°, 55.23°	10 km	6.0	103°, 52°, 98° 271°, 39°, 80°
	USGS	21:32:08	26.942°, 55.227°	10 km	6.0	95°, 51°, 83° 286°, 39°, 98°
A2	GEOFON	23:24:13	26.85°, 55.29°	10 km	5.9	-, -, - -, -, -
	USGS	23:24:14	26.920°, 55.219°	10 km	5.7	96°, 47°, 100° 262°, 47°, 80°
A3	gCMT	23:25:15	26.69°, 55.13°	12 km	6.1	121°, 45°, 138° 245°, 62°, 54°
	GEOFON	23:25:15	26.82°, 55.33°	10 km	6.0	110°, 22°, 118° 261°, 71°, 79°
	USGS	23:25:15	26.887°, 55.285°	10 km	6.0	94°, 34°, 96° 267°, 56°, 86°
Sequence B: 23 July 2022						
B1	gCMT	16:07:56	26.65°, 55.52°	12 km	5.5	56°, 59°, 34° 307°, 62°, 144°
	GEOFON	16:07:49	26.75°, 55.28°	10 km	5.3	82°, 33°, 108° 240°, 59°, 79°
	USGS	16:07:48	26.880°, 55.210°	10 km	5.3	126°, 35°, 133° 258°, 65°, 65°
B2	gCMT	16:09:08	26.73°, 55.22°	12 km	5.6	128°, 65°, 148° 233°, 61°, 29°
	GEOFON	16:09:08	26.98°, 55.52°	10 km	5.5	120°, 48°, 140° 240°, 61°, 50°
	USGS	16:09:07	27.002°, 55.366°	10 km	5.4	121°, 58°, 150° 228°, 64°, 36°
Sequence C: 30 November 2022						
C1	gCMT	15:17:43	26.69°, 55.21°	12 km	5.6	107°, 54°, 101° 270°, 40°, 77°
	GEOFON	15:17:43	26.83°, 55.29°	10 km	5.6	101°, 68°, 91° 278°, 22°, 28°
	USGS	15:17:41	26.887°, 55.239°	5 km	5.6	94°, 65°, 86° 285°, 26°, 99°

Agencies:
gCMT - Global CMT (Dziewoński et al., 1981; Ekström et al., 2012)
GEOFON - GEOFON program using data from the GEVN partner networks (Quinteros et al., 2021)
USGS - USGS National Earthquake Information Center, PDE

from local to teleseismic. We also aim at understanding the interaction of main- and aftershocks in the region using relocated aftershocks. The joint analysis of different data sets and main- and aftershocks shall provide deeper insights into source mechanisms and rupture kinematics of the mainshocks. Our work complements studies focusing on satellite deformation data (e.g., Yang et al., 2023) by resolving temporal aspects and rupture parameters and constraining the position of the activated fault system from aftershocks.

2 Materials and methods

We want to understand the characteristics of the July–November 2022, SE Iran, mainshocks (Tab. 1) from point and finite fault inversions using seismic and, if available, satellite deformation data. Complementing our analyses we relocate aftershocks to gain insights into the stress transfer and the activation of fault planes caused by the mainshocks. In the following, we introduce the pre-processing applied to the satellite deformation data. This dataset is used in the joint multiple source inversions. We also explain the settings of the single- and multiple-earthquake-inversion approaches for the point source and the finite fault models, which are used to study the mainshocks. Furthermore, the methodology for an independent measure of the focal depth based on teleseismic body wave phases is presented. Finally, a brief introduction of the aftershock relocation is given.

2.1 InSAR data pre-processing

Interferometric Synthetic Aperture Radar (InSAR) surface displacement measurements are crucial to constrain earthquake locations, particularly in finite fault inversions (e.g., Ide, 2007; Steinberg et al., 2020). For our multisource inversion approaches, we use interferograms recorded on Sentinel-1. The unwrapped and geocoded interferograms were obtained from an ascending orbit (track 130, 22 June 2022, to 04 July 2022) and a descending orbit (track 166, 25 June 2022, to 07 July 2022), each with a 12-day temporal baseline, via the COMET-LiCSAR web portal along with essential metadata and coherence data. The Generic Atmospheric Correction Online Service (GACOS) offers tropospheric delay products (Yu et al., 2017, 2018b,a), which aim at reducing tropospheric noise in interferograms. However, due to the negative impact of GACOS-based corrections on unwrapped interferograms, we opted to employ a linear method that leverages the correlation between phase and elevation for stratified tropospheric noise correction (Doin et al., 2015).

We processed InSAR time series for the tracks 130 (ascending) and 166 (descending) using the open-source Miami InSAR time-series software in Python (`MintPy`, Yunjun et al., 2022) and the Hybrid Pluggable Processing Pipeline (HyP3) service (Hogenson et al., 2016). HyP3 is a cloud-native infrastructure that offers a generic processing platform for SAR data, including interferometric processing. It streamlines the generation of interferograms, coherence maps, and unwrapped phase products by automating the necessary processing steps. The HyP3 service facilitated our processing of Sentinel-1 data, enabling consistent and efficient generation of interferometric products. The results demonstrated similar deformation patterns for both ascending and descending tracks, providing consistency and confidence in our findings.

Corrected displacement maps are post-processed using the software toolbox Kite (Isken et al., 2017) (Fig. 3). Post-processing includes an empirical variance-covariance estimation of the data error as an input for data weighting within the later inversion (Sudhaus and Jónsson, 2009) and irregular quadtree subsampling (Jónsson et al., 2002) (Fig. 7).

2.2 Bayesian moment tensor (MT) inversion of the mainshocks

We performed moment tensor (MT) point source inversions on both the individual mainshocks and also jointly on the whole sequence A using the Bayesian inversion software Grond (Heimann et al., 2018). Utilizing a particle swarm method combined with bootstrapping, Grond estimates non-linear uncertainties of all inversion parameters. We fit the MT components (full and deviatoric for the individual source inversions and double couple (DC) for the joint inversion), centroid loca-

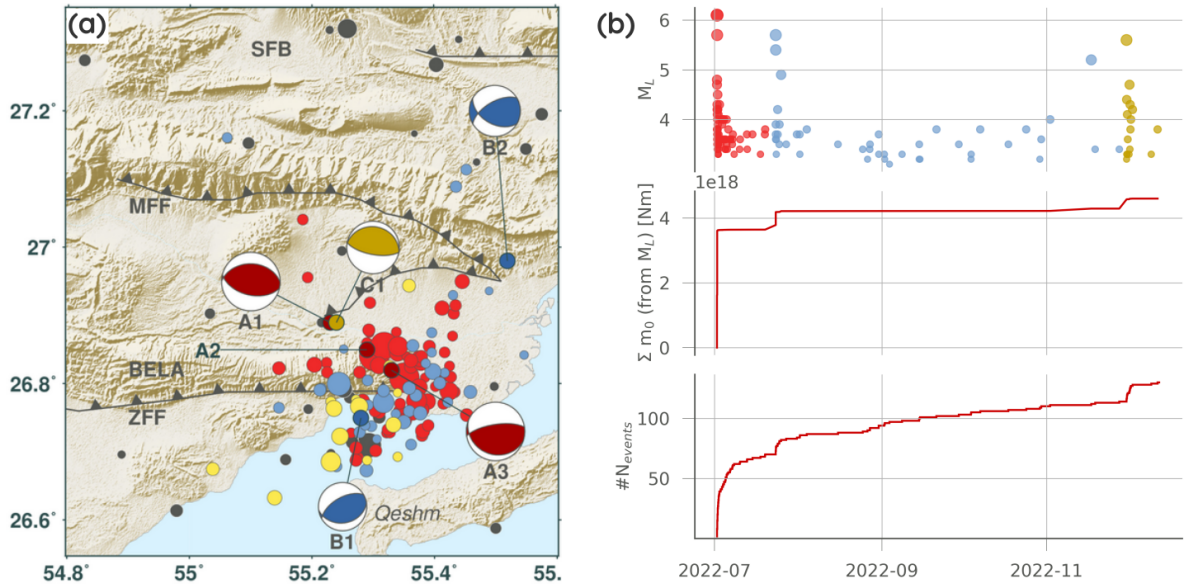

Figure 2 (a) Seismicity from IRSC in Southern Iran before 01 July 2022 (grey dots) and after (colored dots), including GEOFON MT solutions (or location for A2) for the mainshocks. Colors of the dots and MTs indicate the time after 1 July (red), after 22 July (blue), or after 30 November (yellow), respectively. (b) shows the temporal seismicity evolution (mL, cumulative moment, and the number of events) using the IRSC catalog with the same color coding as in (a). Major tectonic/seismic features highlighted/annotated in (a) are the Mountain Front Fault (MFF), the Zagros Foredeep Fault (ZFF), the Simply Folded Belt (SFB), and the Bandar-e-Lengeh anticline (BELA).

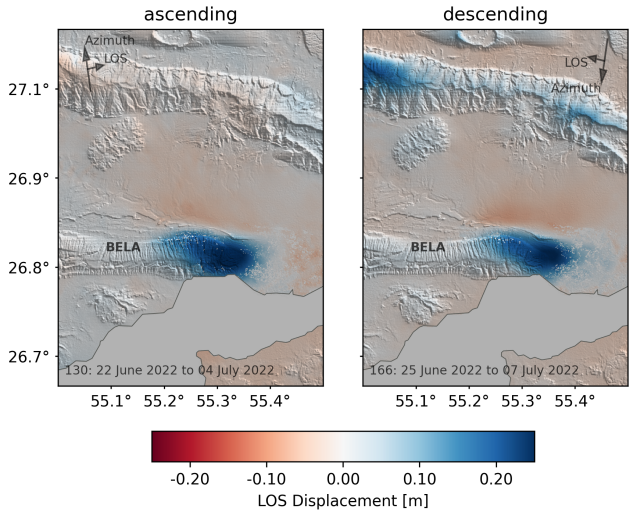

Figure 3 Ground deformation derived from satellite data from ascending (left) and descending tracks of Sentinel 1. Track ID and acquiring dates are shown in the bottom left. The line of sight (LOS) and satellite track (azimuth) directions are indicated by arrows. The displayed deformation is used as input for the joint inversions. BELA indicates the Bandar-e-Lengeh anticline.

tion, time, and duration based on waveform and static ground displacement fits.

Individual earthquake inversions used teleseismic and regional body wave signals, recorded at 18 teleseismic and seven regional stations with an epicentral distance of ∼230–10 000 km with carefully selected time windows to ensure less overlap between the signals emitted by subsequent earthquakes. Due to inaccessible regional data, all inversions for C1 used only the teleseismic dataset. Before inversion, data was visually inspected, and all noisy, incomplete, or corrupted signals were removed. All waveforms have been fitted as bandpass-filtered displacements (0.015–0.06 Hz for A1 and A3, 0.02–0.06 Hz for A2, B1, B2, and C1) in time domain on the vertical and transverse components. Lower frequency limits were chosen to suppress low-frequent noise. Relatively low upper-frequency limits diminish high-frequent site effects and reduce the effect of structural inhomogeneities not captured within our ground model on the data fit. Synthetic waveforms were generated based on Green's functions calculated with QSEIS (Wang, 1999) using the AK135 global and a regional velocity model (Karasözen et al., 2019; Jamalreyhani et al., 2021).

A joint inversion scheme described as the double DC or double single force source by Carrillo Ponce et al. (2021) was adapted and then used for the earthquakes of sequence A. The original approach allows for simultaneous source estimates via parameterizing the temporal and spatial distance between subevents with the focus on single, but complex earthquakes. It subsequently enables the use of seismic records characterized by overlapping signals of different subevents. Furthermore, ground displacements recorded by InSAR with their coarse temporal resolution can be fitted to the superposed synthetic ground displacements of all inverted subevents.

The mentioned double DC inversion scheme was enhanced for simultaneous inversions of three earthquakes as required for a complete assessment of sequence A. These inversions used seismic and satellite deformation data within separate and joint runs. Satellite deformation data was fitted to synthetic ground displacements calculated with PSGRN and PSCMP (Wang

et al., 2003; Wang, 2005; Wang et al., 2006) using the regional velocity model by Karasözen et al. (2019); Jamalreyhani et al. (2021). An interpretation of the triple source inversion must be done with care as more free parameters within the inversion may also lead to overfitting or the fitting of noise signals. The double source setup could not be applied to sequence B due to high noise levels on the satellite deformation.

Throughout this paper, we will always refer to the mean model and the standard deviations derived from the inversions.

2.3 Bayesian inversion of the finite faults

Extended rupture characteristics have been estimated using the pseudo-dynamic rupture (PDR) (Metz, 2019; Dahm et al., 2021). This extended rupture model depends on a flexible boundary element method based on Okada (1992) to iteratively estimate the instantaneous dislocation on the fault from a prescribed stress drop behind a moving rupture front. The rupture front propagation is estimated using the 2D Eikonal equation and the rupture velocity linearly scaling with the shear wave velocity of the regional velocity model by Karasözen et al. (2019); Jamalreyhani et al. (2021). The further parametrization was chosen as in Metz et al. (2022) fitting 13 parameters per fault: the top edge location (lat, lon, depth), the rupture orientation (strike, dip), length and width of the rupture plane, the maximum shear slip, the rake, the relative origin coordinates, the origin time, and the scaling factor between the rupture and shear wave velocity.

The inversion settings are the same as for the MT inversions using individual and joint inversion approaches. Due to the lack of regional data for C1 and noisy satellite deformation records for sequence B, we performed PDR inversions only on the earthquakes of sequence A.

2.4 Focal depth estimation from teleseismic depth phases

We want to validate the depth estimates of our point source and finite fault inversions. Here, we apply a technique for an accurate focal depth computation based on the teleseismic delay between direct P phases and surface reflected, pP, phases using the abedeto tool (https://github.com/HerrMuellerluedenscheid/abedeto). Using the arrival time difference between the two phases (pP-P) recorded on several arrays at teleseismic distances (Fig. S18, Tab. S6 in supplementary material), we independently calculated the focal depth for the six greatest events as previously applied in the Zagros region (Jamalreyhani et al., 2021). The observed waveforms are stacked for each array to increase the signal-to-ratio. In order to create synthetic waveforms, first Green's functions are computed using a reflectivity approach (QSEIS; Wang, 1999) by taking into account the moment tensors calculated in this study. The Green's functions are based on local crustal velocity models at the source and array locations (CRUST2.0; Bassin et al., 2000), and a mantle model (AK135; Kennett et al., 1995).

2.5 Relocation of aftershocks

Earthquake relocation is vital to improve the spatial resolution of seismic sequences. We used the GrowClust3D.jl relocation method (Trugman and Shearer, 2017; Trugman et al., 2023), which implements a cluster-based relocation scheme based on relative time shifts between P- and S-wave arrivals of events with similar waveforms. The method requires a high waveform similarity among the different events and clustered initial locations.

Time shifts are converted into distance and azimuths using pre-calculated travel times based on a 1D velocity model; the required ray tracing was performed using the same regional ground model as for the inversions (Karasözen et al., 2019; Jamalreyhani et al., 2021). Due to limitations in waveform data access, we adopted the scheme to handle picked Pg, Pn, Sg, and Sn arrivals derived from the IRSC catalog. Required relative time shifts for two events were obtained by subtracting absolute arrival times for matching stations.

This approach allows getting a first-order relocation of the catalog with the limitations caused by the arrival time picks provided only to the tenth of a second and the lack of quality control parameters like the cross-correlation coefficient. In total, 120 aftershocks of all three sequences A, B, and C with mL larger than 3.0 from 01 July 2022 until 12 December 2022 were relocated (Fig. 2).

3 Results

In the following we will summarize our findings. We start with the pure seismic inversions of both point and finite source models. Thereafter, results from the joint satellite deformation and seismic data inversions are presented. We will also show results from the focal depth estimation. Finally, outcomes from the aftershock relocation are shown. Due to indications for dominant southward dipping thrusting (Yang et al., 2023) we will discuss our point source results emphasizing the south-dipping nodal planes.

The analysis of seismic data yields robust MT solutions for seven events with M_w larger than 5.3 from 01 July 2022 to 30 November 2022 (Figs. 4a,b, S1–S6, Tabs. 2, S1, S2). All indicate rupture on E-W striking planes (88°–118°) with one focal plane dipping with 37°–68° towards the South. Dips vary from shallow 37°–39° (A3, B1) to more than 60° (A1, B2, C1). While events A1, A2, and C1 show rather pure thrust (rake of 80°–100°), events A3 (rake of 120°) and especially B1 and B2 (rake of 132°–142°) indicate oblique faulting. The magnitudes of the events range from 5.27 for event B1 to 6.01 for event A3 with the highest magnitudes observed for sequence A (M_w 5.73–6.01). All centroids of sequence A are located close to each other beneath or slightly to the North of the Bandar-e-Lengeh anticline (BELA) in depths of 6.8–8.0 km. B1 and B2 occurred in larger depths of 10.4–11.5 km, with B1 being co-located with sequence A and B2 shifted by 10 km towards the North. The later event C1 shows a strong location migration towards the West by ≈20 km. Its centroid lays

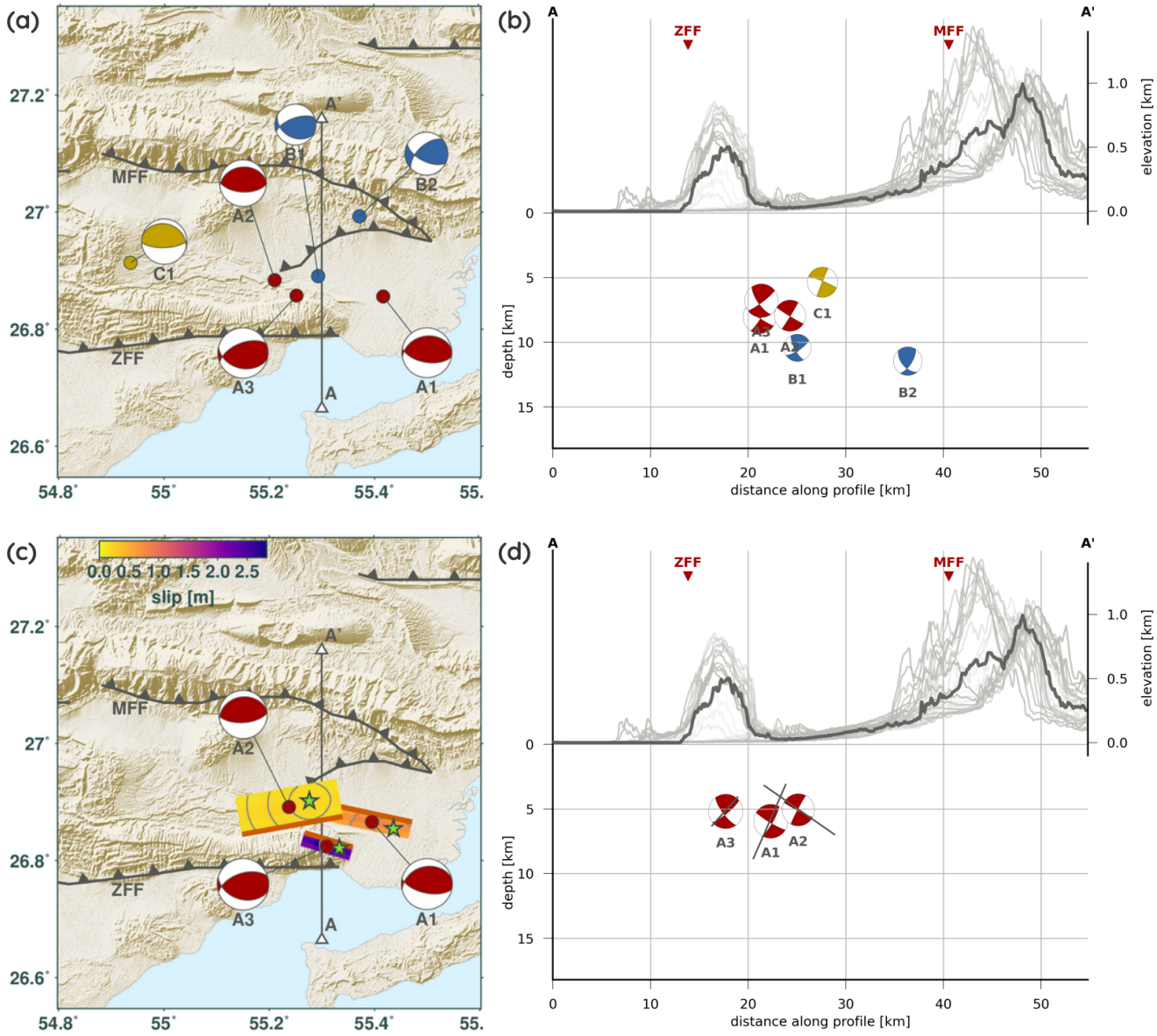

Figure 4 Results of seismic inversions with centroids from full MT inversions as map (a) and along the profile (b). PDR inversion results using seismic data are shown as map (c) and profile (d) with their centroids (dots), rupture plane locations, final slip, rupture origin (green star) and rupture propagation contour lines (every 2 s, grey lines in (c)). Grey lines in (d) indicate the PDR rupture plane locations and orientations through their respective centroids. The topography in the profiles (b, d) is shown along the profile A–A' (dark grey) and along parallel lines extracted every $0.01°$ longitude from $55.15°$W to $55.45°$W (light grey). Increasing transparency scales with increasing distance to the profile A–A'.

beneath the BELA at a shallow depth of $5.4\,\mathrm{km}$.

Independent finite fault solutions obtained from seismic data for sequence A yield preferred orientations of the fault plane but with minimal misfit differences compared to the inversions for the auxiliary nodal plane (Figs. 4, S7–S9, Tabs. 2, S4). Preferred fault planes strike towards West ($260°$) and dip towards North by $28°$ for A2 or strike East ($102°$–$107°$) with a southward dip of $41°$–$61°$ for A1 and A3. Rakes of $85°$–$115°$ indicate pure thrust faulting with a slight oblique component for A3. Source plane extents range from $9.5 \pm 2.3\,\mathrm{km} \times 3.4 \pm 1.5\,\mathrm{km}$ in length and width for A3 up to $19.3 \pm 3.0\,\mathrm{km} \times 8.1 \pm 1.3\,\mathrm{km}$ for A2. Resolved top edge depths are similar through all events of sequence A ranging from $3.1 \pm 0.7\,\mathrm{km}$ for A1 to $4.1 \pm 0.6\,\mathrm{km}$ for A3 (Tab. S4). Significant uncertainties indicate a poor resolution of the rupture origin location and hence the rupture propagation. However, all events of sequence A yield prevailing westward motion along the respective fault planes. Centroids derived from the PDR are similar to the MT solutions in location, magnitude, and orientation. Inferred centroid depths are slightly smaller, with 5.2–$6.2\,\mathrm{km}$. Also, the magnitude estimate for event A2 deviates from the MT solutions with M_w 5.87 compared to 5.73 ± 0.03.

Modeled waveforms show a high fit in amplitude and phase for both CMT and PDR inversions (Figs. 6 top row, S1–S9). PDR fits of the mean model of A1 indicate an overestimation of the amplitude at the displayed station GE.SANI. Fits for the later event A2 are characterized by a slight amplitude deficit of the modeled compared to the observed waveforms for both PDR and CMT solu-

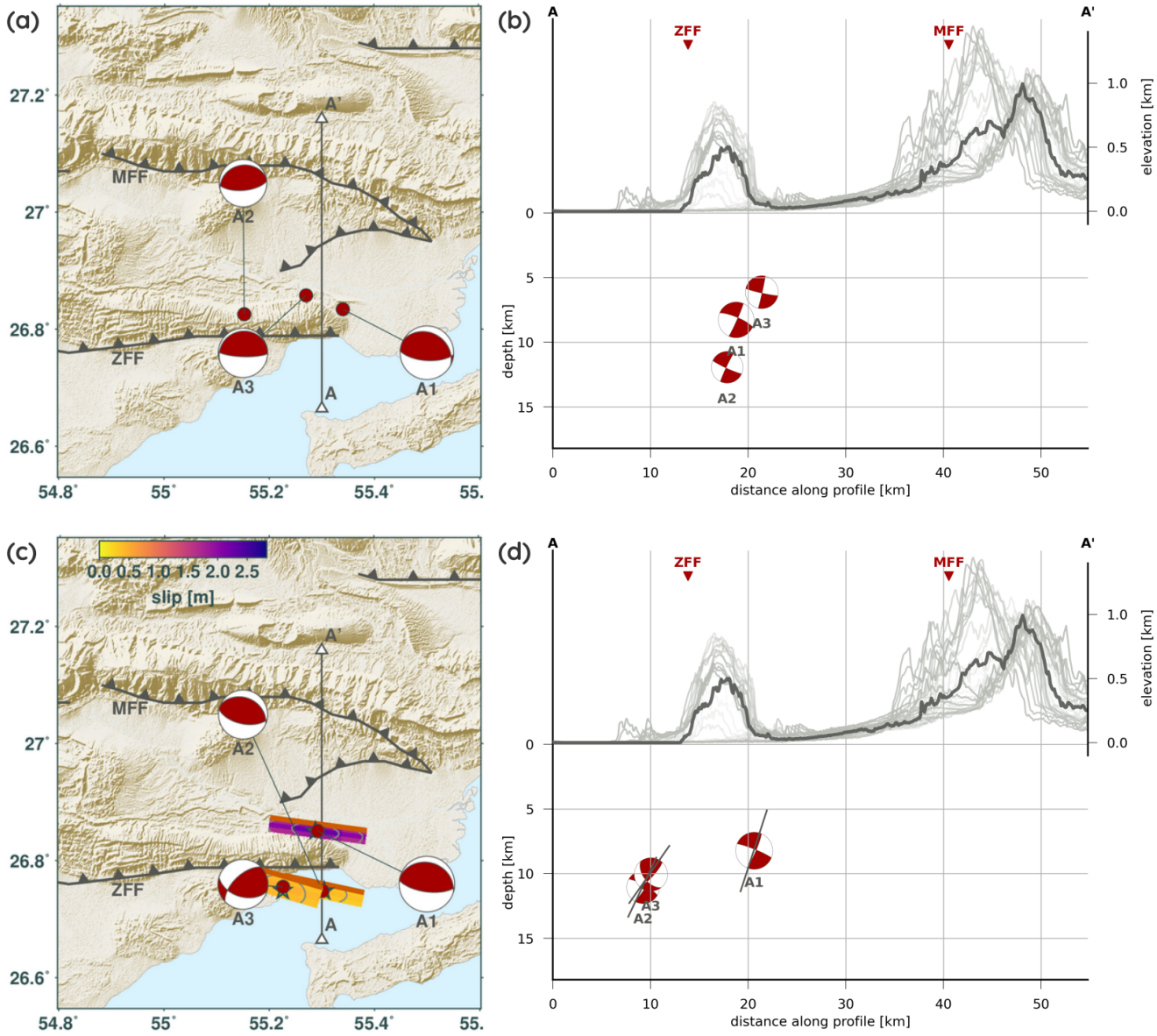

Figure 5 Results of joint seismic and satellite deformation data inversions with centroids from joint 3 DC inversion as map (a) and along the profile (b). Joint PDR inversion results using seismic and satellite deformation data are shown as map (c) and profile (d) with their centroids (dots), rupture plane locations, final slip, rupture origin (green star) and rupture propagation contour lines (every $2\,\mathrm{s}$, grey lines in (c)). Grey lines in (d) indicate the PDR rupture plane locations and orientations through their respective centroids. The topography in the profiles (b, d) is shown along the profile A–A' (dark grey) and along parallel lines extracted every $0.01°$ longitude from $55.15°$W to $55.45°$W (light grey). Increasing transparency scales with increasing distance to the profile A–A'.

tions.

For sequence A, joint inversions were carried out using seismic and satellite deformation data within a triple source inversion scheme. The triple source inversion accounts for the limited temporal resolution of satellite deformation data, which only measures the overlapping effect of the three sources. The triple DC point source inversion fits the seismic, and the satellite deformation data and yields results in agreement with our previous seismic inversions (Figs. 5a,b, 6, 7a,b, S10, Tabs. 2, S3). All mechanisms indicate thrust faulting along an E-W striking plane. The MT for A3 shows a significantly smaller oblique proportion and a much larger dip towards the South ($78°$) of one of its nodal planes compared to the similarly oriented plane of the pure seismic inversion ($39°$). The moment release indicates the highest magnitude for A1 with M_w 6.27, which is about 0.3 magnitude units larger than the magnitude estimate for A1 from the pure seismic single source inversion. Synthetic waveforms (Figs. 6, S10) show significantly larger amplitudes compared to the observed and the synthetic traces from the pure seismic inversion (Fig. S1), suggesting that the satellite deformation data forces the seismic moment of A1 to have larger values. On the other hand, magnitude estimates for A2 and the corresponding waveform fits are similar to the observed traces. Finally, waveform amplitudes and the magnitude for A3 are underestimated when compared to the observed traces and the seismic modeling, respectively.

In general, the locations of the centroid double cou-

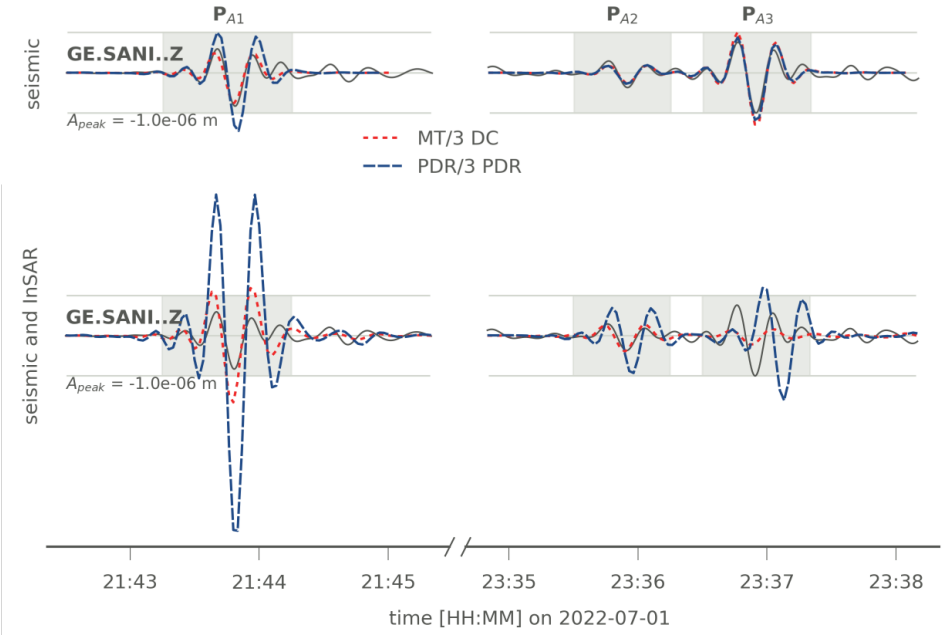

Figure 6 P-wave fits for sequence A (left A1, right A2 and A3) displayed on the vertical displacement records of station GE.SANI (distance $\approx 8215\,\mathrm{km}$, azimuth $\approx 119°$) for seismic (top row) and joint inversions (bottom row). Observed, restituted and filtered records are given in black, fitted traces in colored lines. Horizontal grey lines indicate the peak amplitude of the observed records with the value given as A_{peak}. Grey background with the top labels indicate the major P-wave signal of the different events.

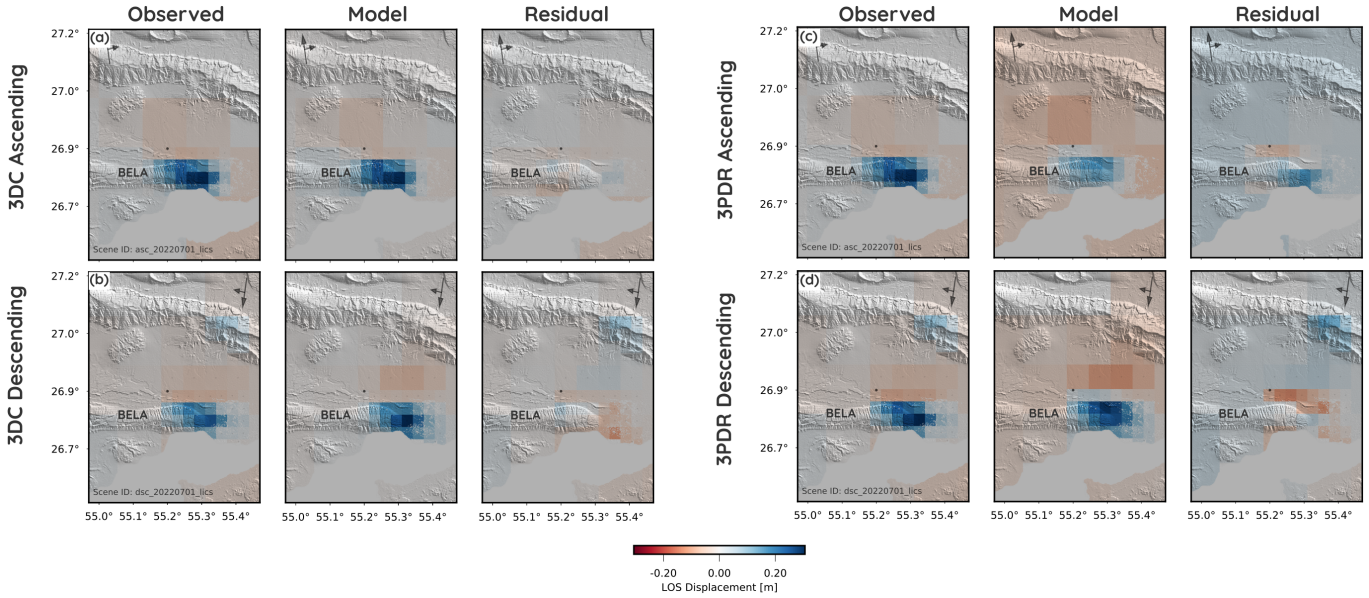

Figure 7 InSAR fits for joint 3DC (ascending - a, descending - b) and 3PDR (ascending - c, descending - d) inversions with quadtree subsampled observed data (1st column), the mean model fit (2nd column) and the corresponding residual (3rd column). BELA indicates the Bandar-e-Lengeh anticline.

ple MTs are resolved well with the largest errors for A2 (max. $5.1\,\mathrm{km}$ horizontal and 2.7 vertical error - Tab. S3). The depth of A2 ($11.9\,\mathrm{km}$) is significantly larger than estimated from seismic data ($7.9\,\mathrm{km}$).

The joint inversion of three PDR finite fault planes yields stable estimates, especially for A1, with more significant uncertainties for A2 and A3. All events are characterized as E-W striking thrust earthquakes with south dipping source planes (Figs. 5c,d, 6, 7, S11, Tabs. 2, S5). Fault orientations are mainly in agreement with results from the other inversion approaches. Contrary to the single PDR inversion, the joint inversion favors a south-dipping fault plane for A2. For A3, we obtain a large oblique component but with larger uncertainties (rake of $134° \pm 22°$) compared to point source and single finite fault inversions. The estimated seismic moment from the mean model centroid defines A1 as the largest event with M_w 6.42 and a maximum shear dislocation of $2.26 \pm 0.37\,\mathrm{m}$, while A2 and A3 released a moment equivalent to M_w 5.91 (slip of $0.39 \pm 0.20\,\mathrm{m}$) and

M_w 5.98 (slip of 0.50 ± 0.24 m). For A1 and A2, both magnitudes and maximum dislocations are overestimated compared to all other inversion approaches. The largest magnitude (> 0.4 magnitude units), and slip increase ($\sim$1.4 m), compared to the single point source or PDR seismic inversions, is observed for A1.

Waveform fits (Figs. 6, S11) indicate good phase retrieval, especially for A1 and A2. Slight phase shifts are observable for some records of A3. Similarly to the triple DC inversion, we obtain an amplitude overestimation for A1, but here even more prominent. In general, waveform amplitudes for A2 and A3 fit well.

Satellite deformation data shows a high correlation in the estimated deformation pattern with residuals of $\sim$10 cm. The ascending track fit is characterized by an underestimation of the maximum deformation measured at the BELA. In contrast, the descending track shows larger residuals along the NE boundary of the BELA (Fig. 7c,d). Both, centroid location and depth of A1 beneath the northern edge of the BELA are in good agreement with solutions from the other inversion approaches. Centroids of A2 and A3 are co-located south of the BELA beneath the Tangeh Khoran, indicating a shift of $\sim 10 \pm 8$–9 km towards the South compared to the other inversion results (Tab. S5). The respective depths are in the range of 10.1–11.1 km, up to 6 km larger than the results from our other inversion approaches.

Focal depths of the mainshocks estimated from P-wave phase arrival time differences are in the range of 7.0–11.0 km (Figs. S12–S17, Tabs. 2, S6). Smallest focal depths are obtained for C1 (7.0 km), and A1 and A2 (8.0 km). The origin depth for A3 is estimated with 10.0 km, while largest focal depths of 11.0 km are found for B1 and B2. The stacked waveform fits are rather good for the smaller events B1, B2, and C1. The larger events of sequence A generate more complex P-waves due to a longer rupture duration and, hence, source time functions. Therefore, stacked waveform fits are not as good as for the smaller events.

120 aftershocks of the IRSC catalog from 01 July 2022 to 12 December 2022 have been relocated with average vertical (depth) and horizontal location shifts and uncertainties of 0.41 ± 0.39 km and 0.67 ± 0.82 km, respectively (Figs. 8, S19, Tab. S7). The simultaneous optimization of the origin times yields an average shift of 0.1 ± 0.1 s. The majority of events are located in depths of 10–15 km scattering within a $\sim$10 km $\times$ 10 km wide area around 26.8° lat, 55.35° lon. They are characterized by minor location errors (Fig. S12). Larger errors in the relocation of up to 3 km horizontally and 2 km in depth are observed for the few events located towards the North and SW of the major aftershock area. The location of most aftershocks fits well with inversion results from both MT and PDR inversions, except the MT solution of C1. The westward location shift of C1 compared to sequences A and B (Fig. 4) is not reflected in the relocated aftershocks. We also do not resolve any scattering of aftershocks along preferred planes.

4 Discussion and interpretation

The analyzed earthquakes between 01 July 2022 and 12 December 2022 highlight the interaction of large, shallow thrust earthquakes in the sedimentary layer with smaller aftershocks in the upper basement or deeper sedimentary cover (Fig. 9), which is a peculiarity of the continent-continent collision in the Zagros Mountains (see e.g., Nissen et al., 2011, 2014). Using different inversion approaches, we can also resolve significant differences in the earthquake parameter estimates due to uncaptured tectonic processes or uncertainties in the used ground models. In the following, we will discuss our results related to regional tectonics, the effect of the incorporated satellite deformation data and its seismological implications, and the quality of the newly developed triple source inversion scheme.

4.1 Mainshock mechanisms and location

The earthquakes in Zagros generally have low to strong magnitudes up to M_w 7.3 and commonly occur on blind faults (Barnhart et al., 2013; Karasözen et al., 2019; Asayesh et al., 2022; Jamalreyhani et al., 2022; Nissen et al., 2019), often in depths of 8–14 km (e.g., Ni and Barazangi, 1986; Baker et al., 1993; Hessami et al., 2001; Talebian and Jackson, 2004; Jamalreyhani et al., 2021; Nissen et al., 2019). Ruptures often occur in the sedimentary layer, called a "competent group", which spans from $\approx$4–8.5 km depth in the south eastern FA. The competent group is decoupled from the crystalline basement by the Hormuz Salt Formation at about 8–10 km (Nissen et al., 2011), a formation intercalated with stronger non-evaporitic layers. The centroids of the earthquakes A1, A3, and C1 locate in a depth of 5–8 km depth (Figs. 4, 5), which indicates an activation of faults in the lower competent group. This interpretation is supported by Roustaei et al. (2010); Nissen et al. (2010, 2011); Barnhart et al. (2013); Elliott et al. (2015) who found that most $M_w > 5$ events occur in the shallow sedimentary layer between $\sim$5–10 km. Estimated focal depths for A1, A3, and C1 of 7.0–10.0 km are in line with results of our inversion and of the given studies (Tab. 2).

The later earthquake sequence B (and perhaps also A2) occurred at a larger depth of 10.5–11.5 km, shown by both centroid and focal depths, indicating a possible stress transfer from the shallow primary events A1 and A3 into depth with an activation of the deeper sedimentary Hormuz layer, interface between sediments and basement and/or faults within the crystalline basement. Both, stress transfer and the activation of significantly deeper strata are also evident from the aftershock depth range of 10–15 km below the Bandar-e-Lengeh anticline (BELA), which fits well with earlier estimates of aftershock depths, e.g., for the 2005 Qeshm or 2006 Fin earthquakes (e.g., Talebian and Jackson, 2004; Tatar et al., 2004; Nissen et al., 2011; Yaminifard et al., 2012). The scenario of a shallow mainshock followed by a separated, deeper aftershock sequence has been observed and described by Nissen et al. (2011); Yaminifard et al. (2012) for the 2005 Qeshm earthquake. The pattern may indicate that characteristic earthquakes in

Table 2 Centroid locations and orientations derived from MT and PDR inversions using both seismic and a joint seismic and InSAR dataset. The ensemble mean solution is given. Full set of resolved parameters including uncertainties are given in Tables S1–S5. Also, results from teleseismic focal depth estimation are given.

ID	Method	Time	Lat, Lon	Depth	M_w	max. Slip	Strike, Dip, Rake
Sequence A: 01 July 2022							
A1	MTs	21:32:08.7	26.856°, 55.417°	8.0 km	5.97	-	100°, 58°, 101°
							260°, 33°, 83°
	MTj	21:32:06.3	26.835°, 55.340°	8.3 km	6.27	-	94°, 66°, 79°
							299°, 26°, 113°
	PDRs	21:32:08.8	26.861°, 55.390°	6.2 km	5.96	0.82 m	102°, 61°, 102°
	PDRj	21:32:09.4	26.851°, 55.292°	8.2 km	6.42	2.26 m	98°, 67°, 87°
	TELE	-	-	8.0 km	-	-	-
A2	MTs	23:24:14.8	26.884°, 55.210°	7.9 km	5.73	-	93°, 59°, 95°
							264°, 32°, 83°
	MTj	23:24:15.7	26.826°, 55.153°	11.9 km	5.78	-	85°, 65°, 94°
							256°, 25°, 82°
	PDRs	23:24:14.6	26.896°, 55.234°	5.2 km	5.87	0.24 m	260°, 28°, 85°
	PDRj	23:24:11.6	26.748°, 55.301°	11.1 km	5.91	0.39 m	102°, 59°, 86°
	TELE	-	-	8.0 km	-	-	-
A3	MTs	23:25:14:3	26.858°, 55.252°	6.8 km	6.01	-	104°, 39°, 120°
							248°, 57°, 69°
	MTj	23:25:15.5	26.858°, 55.270°	6.1 km	5.93	-	92°, 78°, 95°
							251°, 13°, 69°
	PDRs	23:25:14.5	26.838°, 55.272°	5.6 km	5.98	2.83 m	107°, 41°, 115°
	PDRj	23:25:20.9	26.756°, 55.226°	10.1 km	5.98	0.50 m	106°, 48°, 134°
	TELE	-	-	10.0 km	-	-	-
Sequence B: 23 July 2022							
B1	MTs	16:07:47.6	26.891°, 55.293°	10.4 km	5.27	-	118°, 37°, 132°
							250°, 64°, 64°
	TELE	-	-	11.0 km	-	-	-
B2	MTs	16:09:07.8	26.993°, 55.372°	11.5 km	5.42	-	116°, 60°, 142°
							227°, 58°, 36°
	TELE	-	-	11.0 km	-	-	-
Sequence C: 30 November 2022							
C1	MTs	15:17:46.9	26.914°, 54.936°	5.4 km	5.63	-	88°, 68°, 83°
							286°, 23°, 107°
	TELE	-	-	7.0 km	-	-	-

Methods:

MTs - Full moment tensor inversion from seismic data.

MTj - Joint inversion of triple DC sources from seismic and InSAR data.

PDRs - PDR inversion from seismic data.

PDRj - Joint inversion of triple PDR sources from seismic and InSAR data.

TELE - Focal depth estimation from teleseismic depth phases.

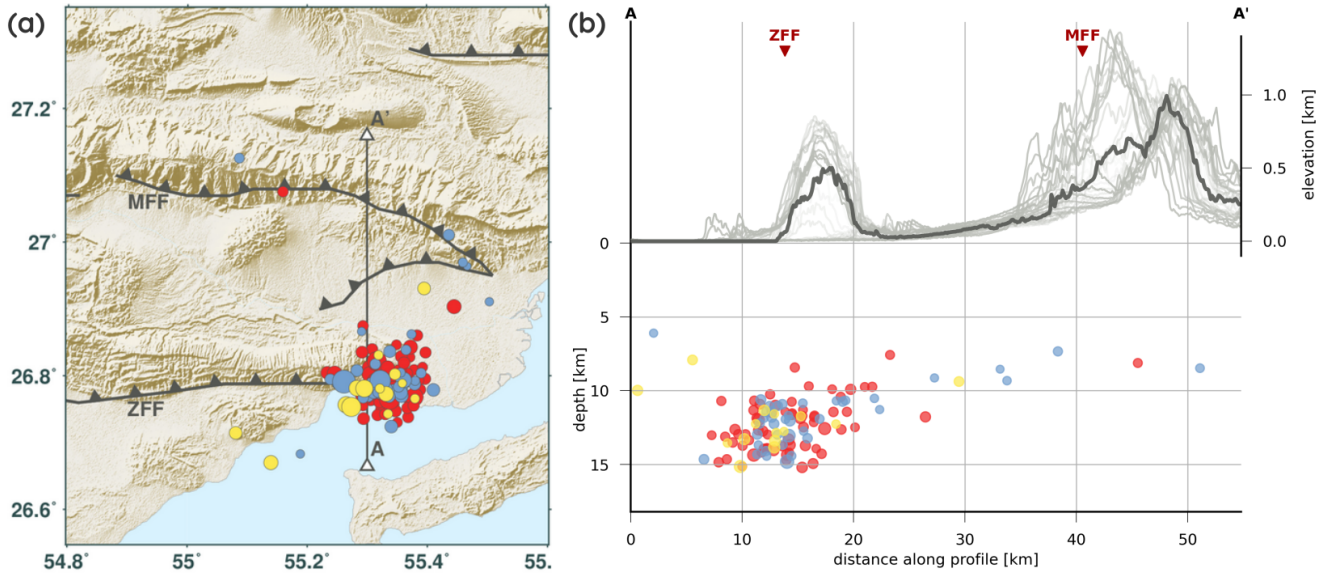

Figure 8 Map (a) and profile (b) of the IRSC catalog after relocation between 01 July 2022 and 12 December 2022. Mainshocks of sequences A, B and C are excluded. Colors indicate the time after sequence A (red), B (blue) or C (yellow). Points scale with reported local magnitude. The topography in the profile (b) is shown along the profile A–A' (dark grey) and along parallel lines extracted every $0.01°$ longitude from $55.15°$W to $55.45°$W (light grey). Increasing transparency scales with increasing distance to the profile A–A'.

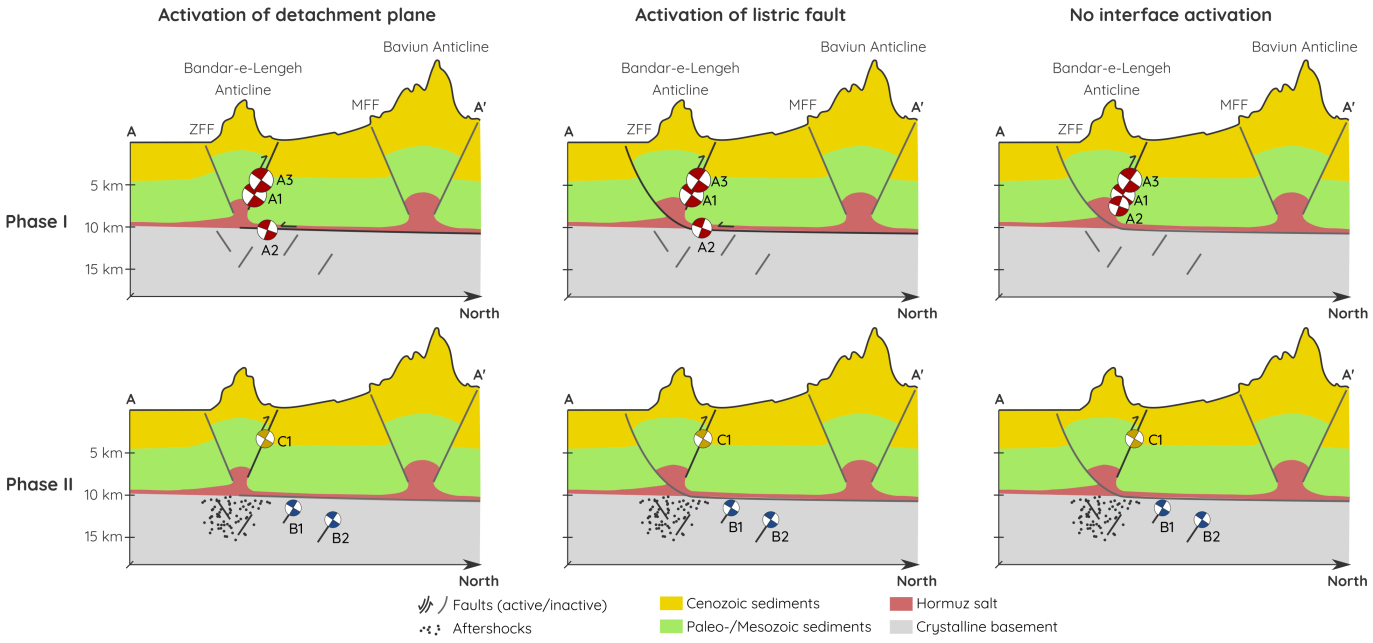

Figure 9 Interpretation of the tectonic processes during the July–December 2022 sequence. Phase I (top row) indicates the rupture processes on the 01 July 2022 while phase II (bottom row) resolves the later events. Moment tensors do not show correct rotations but shall illustrate general trends in location and mechanism. We show three interpretation possibilities using an activation of the detachment plane (left), a listric fault cutting through the sediments (center), or a rupture independent of the sediment to basement interface (right). North is indicated at each profile. The profiles are also referenced to the profile A–A' shown in Figs. 4, 5, and 8.

the competent group of the sedimentary cover are controlled by a combination of stress and forces from the horizontal collision and buoyant salt movements, while the crystalline basement of the crust is moving as a decoupled, rigid body beneath the ZFFB. Aftershocks can be induced in the basement if Coulomb stress changes occur. However, the crustal shortening in the basement is either accommodated by ductile deformation, or through crustal thickening as observed further to the north beneath the HZZ.

In addition to thrust faulting and shortening, transverse strike-slip faults play a role in the evolution of Zagros. For instance, Talebian and Jackson (2004) emphasized the importance of strike-slip faults in the basement of the southeastern-most Zagros, which has also been revealed by Yaminifard et al. (2012) studying after-

shocks of the 2005 Qeshm Island event.

Sequence A is dominated by the two largest thrust events of $M_w \sim 6.0$ (A1 and A3). Satellite deformation data (InSAR) show largest displacements on the BELA and minor deformation towards North (Figs. 3, 7). From the deformation pattern Yang et al. (2023) have derived two southward dipping rupture planes with dips of 33–65°. Despite the steeply dipping planes, no surface ruptures were observed. This is, however, common for thrust events in Zagros mountains (e.g., Berberian, 1995; Regard et al., 2004; Yamini-Fard et al., 2007; Edey et al., 2020). From our joint seismic and InSAR inversion, we found a southward dipping plane of $48° \pm 13°$ (Triple PDR) or $78° \pm 2°$ (Triple DC) (Tabs. 2, S3) for the second large event of sequence A (A3). However, Yang et al. (2023) interpret A3 as a possible southward dipping but low angle, shallow splay fault of A1 with a dip of about 33°.

The results of our single PDR seismic inversions yield similar dip angles as the triple PDR inversion between 41° and 48° on the southward dipping plane, supporting the results by USGS, gCMT, and GEOFON. Prevailing dips for thrust events are up to 60° (Jahani et al., 2009; Nissen et al., 2011). The steep dip estimate of 78° for A3 from the triple DC inversion is well above this range. It could be a result of our triple source inversion setup with many free parameters, allowing for overfitting of small amplitude satellite deformation data (Fig. 7). The poor waveform fits from the triple DC inversion for A3 compared to the single MT inversion support the interpretation of overfitting satellite deformation data at the expense of the waveform data fit (Figs. 6, S3, S10).

Event A2 is characterized by rather good waveform fits (Fig. 6) and comparable solutions through all applied techniques and inversion setups. However, the joint inversions yield a significantly larger centroid depth of 11.1–11.9 km vs. 5.2–7.9 km. The larger depth would imply that A2 ruptured within the upper basement, lower sediments or along their interface. The low-angle northward dipping rupture plane, resolved from PDR inversions, fits well with the latter interpretation of a low-angle detachment earthquake along the interface (Nissen et al., 2011) (Fig. 9 left column). Resolved dips of more than 20° make this scenario unlikely.

Instead of a steeply northward dipping fault plane, the ZFF could also be of listrical shape propagating into the sediment-basement interface as indicated by Jahani et al. (2009) (Fig. 9 center column). Such fault shape could accommodate events with intermediate north dipping focal planes as observed.

A rupture of listric or ramp-flat faults within the basement, as suggested for the 2017 M_w 7.3 Sarpol-e Zahab earthquake (e.g., Fathian et al., 2021; Guo et al., 2022; Zhao et al., 2023) is unlikely in our case. A centroid depth at the top level of the basement and no observable spatial clustering of aftershocks along listric lineaments in the basement, prohibit such interpretation. We also obtain a origin depth of 8 km indicating a rupture within the lower sediments, and not within the basement. Further investigations of the fault geometry, e.g., by using teleseismic body waves (e.g., Braunmiller and Nábělek, 1996), are not easily applicable here due to the rather small magnitude, and hence, the small rupture plane extent of A2, and the complex rheology in the study area, which is not fully reflected in our ground models.

We favor the interpretation of Yang et al. (2023), assuming A2 as a foreshock to A3 on the thrust fault plane of A1 or A3 (Fig. 9 right column). The shallow centroid and focal point depths from seismic inversions and from P-wave phases arrival differences, and the similar focal plane orientations support their hypothesis. Coulomb failure stress changes caused by A1 or A2 on the fault plane of A3 calculated by Yang et al. (2023) also strengthen this interpretation.

Our finite fault inversions with slip estimates for the two largest events of 0.82 ± 0.25 m (single PDR) or 2.26 ± 0.37 m (triple PDR) for A1 and 2.82 ± 0.88 m (single PDR) or 0.50 ± 0.24 m (triple PDR) for A3 support findings on different recent earthquakes in the FA (e.g., for 2005 Qeshm, 2006 Fin, 2008 Qeshm or 2013 Khaki-Shonbe earthquakes) that coseismic slip is mainly accommodated within the competent group (Lohman and Barnhart, 2010; Elliott et al., 2015; Nissen et al., 2007, 2010; Roustaei et al., 2010; Jamalreyhani et al., 2021).

Slips are significantly larger than results from Yang et al. (2023), who estimate peak dislocations of up $\sim$1.25 m. From seismic data, we also estimate different locations for the high slip patch of A1 compared to Yang et al. (2023). It is shifted further to the East with respect to their results. The joint finite fault inversion yields swapped locations of A1 and A3 compared to Yang et al. (2023). While they resolve A1 to the west of A3, we obtain the opposite results. This could be caused by the limited temporal resolution in the study of Yang et al. (2023) as based only on satellite deformation data.

Besides the slip, first-order estimates of the rupture kinematics are obtained from our finite fault inversions. Although shipping with larger uncertainties (Tab. S4), single PDR inversion solutions indicate dominant westward rupture propagation. This indicates that the earlier A1 ruptured into the region of A2 and A3 (Figs. 4, 5).

4.2 Vertical separation of aftershocks

Both, relocated aftershocks, and the larger earthquakes B1 and B2 are spatially concentrated around the eastern tip of the BELA and predominantly scatter in a depth of 10–15 km, which implies aftershock activity is either in the upper crystalline basement (Talebian and Jackson, 2004; Tatar et al., 2004; Nissen et al., 2011) or deeper sediments (Jahani et al., 2009; Nissen et al., 2014). We also see a vertical separation of the aftershocks from the mainshock in the SFB, which fits well with observations by Nissen et al. (2010, 2011, 2014) for the 2005 Qeshm and 2006 Fin earthquakes. While mainshocks rupture the middle-lower sedimentary cover, aftershocks occur in the basement or the deeper sediments within the Hormuz formation. Hence our aftershock locations also indicate a relatively shallow top boundary of this aftershock region at $\approx$10 km depth compared to findings of Nissen et al. (2014).

The co-location of the mainshocks and aftershocks,

despite C1, could highlight Coulomb stress changes, or dynamic stress transfer from the mainshocks into the deeper and harder Hormuz formation (Nissen et al., 2010, 2014). The salt may flow as a response to the stress changes causing aftershocks within the formation and its surroundings. The substantial location shift between C1 and its aftershocks could be due to location uncertainties and poor spatial resolution of our seismic inversion caused by the lack of regional seismic or ground deformation data.

Nevertheless, as derived from travel time picks without quality constraints, our relocations are only valid as a first-order approximation of the aftershock locations. As we used the same ground model for relocation as for the inversions, uncertainties and structural inconsistencies between the model and the actual underground structure might have also caused a bias within the relocation.

4.3 Implications from joint data and multi-source inversion

The newly implemented triple source inversion scheme has proven its usability for complex rupture inversions using multiple satellite deformation and seismic data. We resolved major features of deformation and seismic data, especially when using the triple DC source model. However, additional free parameters in the triple source inversion scheme have also affected the results, as increased centroid depths for A2 and partially A3, larger uncertainties and the large waveform fit residuals, especially for A3. Different weighting schemes for the relative misfit contribution of surface deformation data fits compared to waveform fits were employed to reduce the described effects but did not fully solve this issue. In this regard, our interpretations on the faults activated by A2 can not be validated from the triple source inversion results.

Comparing results from single source seismic and combined source joint seismic and satellite data inversions, we obtain a significant increase in the cumulative moment release with the latter inversion approach (Figs. 4, 5). Our seismic inversions for sequence A yield a cumulative moment release equivalent to M_w 6.24–6.26, similar to results from GEOFON (cumulative M_w 6.29) or USGS with a cumulative M_w 6.25. Meanwhile, our joint inversion approaches give a cumulative moment release equivalent to M_w 6.39–6.52. These values confirm results from Yang et al. (2023), who have obtained a cumulative moment release equivalent to M_w 6.43.

This 60–70 % increase in modeled moment release derived from the triple DC inversion could be caused by a significant afterslip resolved in the satellite deformation data with its broad temporal coverage but not reflected in the seismic data. Observations of afterslip within Zagros reveal a rather large relative contribution to the ground deformation (Zhao et al., 2023) and can yield significant overestimation of the magnitude in the range of 0.1 to > 0.2 magnitude units (Weston et al., 2012). This behavior might be caused by the complex tectonics of the Zagros, e.g., its salt diapirism (Yang et al., 2023).

Another reason for the magnitude differences could be our choice of the ground model. It is specific to the Zagros region (Karasözen et al., 2019; Jamalreyhani et al., 2021). Nevertheless, underground structure variations, as evident from, e.g., Nissen et al. (2011); Jahani et al. (2009); Jamalreyhani et al. (2021) along the Zagros, can not be fully resolved due to the lack of local tomographies. The choice of a rather low-frequency range for waveform fitting reduces such structural effects, though. Nevertheless, local studies, e.g., a tomography using the aftershocks of the sequence combined with seismic profiles, could enhance the knowledge and shed light on this issue.

The significant moment release overestimation by the triple PDR inversion with an increase of 145–165 % compared to the pure seismic inversions may also be influenced by our inversion setup with many free parameters as the larger uncertainties and misfits suggest (Figs. 7, 6, S11, Tabs. 2, S5).

We have resolved a sequence of three earthquakes close in time and space with similar focal mechanisms (sequence A). As likely rupturing the adjacent patches of the same faults or adjacent splay faults (Yang et al., 2023) sequence A can be characterized as an event triplet according to the definition of Lay and Kanamori (1980); Ammon et al. (2008). The sequence highlights a region of large tectonic complexity with overthrusting, opposed dipping splay faults, and the effect of the Hormuz salt formation limiting rupture propagation (Nissen et al., 2011; Jamalreyhani et al., 2023).

Sequence B might be a doublet with its short interevent time and similar mechanisms. We can not resolve if both ruptured on one common fault, though (Figs. 4a,b, 9). Here, a more detailed investigation of stress transfers could help to fully understand this part of the 2022 seismic unrest. Our observations of an event triplet and a possible doublet fit well with recent observations of two other doublets close to our study area (November 2021 Fin and June 2022 Charak - e.g., Nemati, 2022; Fathian et al., 2022; Rezapour and Jamalreyhani, 2022) highlighting the tectonic complexity of the south eastern FA.

5 Conclusions

The 2022 earthquake sequence in SE Iran has revealed a rather complex interaction of larger shallow thrust faults within the sedimentary cover with deeper, smaller events at the interface to and/or within the crystalline basement. The sequence was initialized by a triplet of thrust earthquakes on 01 July 2022. The two largest earthquakes of the triplet (both $\mathrm{M}_w \sim 6.0$) ruptured the lower sediments at depths of 4–9 km, likely occurring on a south-dipping splay fault to the Zagros Foredeep Fault beneath the Bandar-e-Lengeh anticline. The third, smaller, M_w 5.7–5.8 event occurred one minute before the second large event. This small earthquake either indicates an early activation of deeper strata or might also have been a foreshock co-located on the faults, which ruptured during the two mainshocks.

The event triplet caused high aftershock activity within the deeper sediments or upper crystalline base-

ment characterized by depths of 10–15 km beneath the Bandar-e-Lengeh anticline with several larger thrust events. Hence, the 2022 seismic unrest is a new case of observable vertical separation of the main- and aftershocks in SE Iran, which may be caused by a complex stress state within the deeper sediments and the crystalline basement beneath.

Magnitude overestimations when utilizing satellite ground deformation data also indicate a significant afterslip activity due to salt diapirism.

The comprehensive analysis of main- and aftershocks using available seismic and ground deformation data has embedded the July–December 2022 sequence into the complex tectonics in the SE Fars Arc with a frequent occurrence of event doublets over the past year. The lack of regional and local seismic records and the rather uncertain ground models limited the accuracy of our results. This issue highlights the need for further detailed tectonic studies in the region and better data accessibility to properly understand the geophysical processes and their potential risk within the SE Fars Arc.

Conflict of competing interests

The authors declare that the research was conducted in the absence of any commercial or financial relationships that could be construed as a potential conflict of interest.

Contributions of the authors

MM, BMA, MMA, and MJ were involved in the general conceptualization of the study. MM developed and implemented the triple source inversion scheme and performed analysis of the main- and aftershocks. PB performed the focal depth estimation based on teleseismic body wave phases. BAM, MJ, and PB provided the IRSC seismic data and catalog. MMA performed preprocessing of the satellite deformation data and performed subsequent tests on satellite imagery.

MM wrote the original draft with major contributions of BAM and MJ within the introduction and discussion, and of PB within the methods section. MMA provided the methodological overview on satellite data preparation. Images within the draft were generated by MM, BAM, and PB (Fig. 1). MM, BAM, MJ, PB, and TD provided substantial feedback to the draft through their reviews.

TD, and PB have supervised and guided this study.

Acknowledgments

Malte Metz was supported by the BMBF project EWRICA (03G0891B). Behman Maleki Asayesh was funded by the DFG - Research Training Group “NatRiskChange” and Pınar Büyükakpınar is funded by project 407141557 of the Deutsche Forschungsgemeinschaft (DFG, German Research Foundation).

We would like to thank Simone Cesca, Sebastian Hainzl, Sebastian Heimann and Henriette Sudhaus for feedback and guidance on different parts of our study and continuous support. We are also grateful for the helpful comments of Daniel Trugman on the use of the GrowClust3D.jl algorithm.

Data and resources

Our reference source mechanisms were derived from the GEOFON program of the GFZ German Research Centre for Geosciences using data from the GEVN partner networks, global CMT (e.g., Dziewoński et al., 1981; Ekström et al., 2012) and USGS.

The aftershock catalog, body wave travel time picks and regional waveforms were downloaded from the Iranian Seismological Center (IRSC) available at http://irsc.ut.ac.ir/.

Furthermore we used teleseismic waveform data from the following seismic networks: AK (Alaska Earthquake Center, Univ. of Alaska Fairbanks, 1987), DK (GEUS Geological Survey of Denmark and Greenland, 1976), G (Institut de physique du globe de Paris (IPGP) and École et Observatoire des Sciences de la Terre de Strasbourg (EOST), 1982), GE (GEOFON Data Centre, 1993), GT (Albuquerque Seismological Laboratory (ASL)/USGS, 1993), II (Scripps Institution of Oceanography, 1986), IC (Albuquerque Seismological Laboratory (ASL)/USGS, 1992), IN (India Meteorological Department, 2000), IU (Albuquerque Seismological Laboratory (ASL)/USGS, 1988), QZ (LTD Seismological Experience and Methodology Expedition of the Committee of Science of the Ministry of Education and Science of the Republic of Kazakhstan, 2003), RM (Regional Integrated Multi-Hazard Early Warning System (RIMES Thailand), 2008) and WM (San Fernando Royal Naval Observatory (ROA), Universidad Complutense De Madrid (UCM), Helmholtz-Zentrum Potsdam Deutsches GeoForschungsZentrum (GFZ), Universidade De Évora (UEVORA, Portugal) and Institute Scientifique Of Rabat (ISRABAT, Morocco), 1996).

Satellite deformation data was downloaded from LiCSAR. LiCSAR contains modified Copernicus Sentinel data 2022 analyzed by the Centre for the Observation and Modelling of Earthquakes, Volcanoes and Tectonics (COMET). LiCSAR uses JASMIN, the UK’s collaborative data analysis environment (http://jasmin.ac.uk). LiCSAR products can be accessed through the COMET-LiCSAR-portal website at https://comet.nerc.ac.uk/COMET-LiCS-portal/.

Besides the mentioned software we used GMT5.4 for map plotting (Wessel et al., 2013) and their GSHHG dataset for shore lines (e.g., Wessel and Smith, 1996). Topographic data provided by SRTM (Becker et al., 2009) was used for our map and profile plots. Faults plotted were obtained from Hessami et al. (2003). For InSAR processing we used the the Hybrid Pluggable Processing Pipeline (HyP3) platform (Hogenson et al., 2016), while MintPy was utilized as a robust solution for InSAR time series analysis and unwrapping error correction (Yunjun et al., 2022). Furthermore kite was used for satellite deformation data pre-processing (Isken et al., 2017).

References

Alaska Earthquake Center, Univ. of Alaska Fairbanks. Alaska Regional Network, 1987. doi: 10.7914/SN/AK.

Alavi, M. Structures of the Zagros fold-thrust belt in Iran. *American Journal of science*, 307(9):1064–1095, 2007. doi: 0.2475/09.2007.02.

Albuquerque Seismological Laboratory (ASL)/USGS. Global Seismograph Network - IRIS/USGS, 1988. doi: 10.7914/SN/IU.

Albuquerque Seismological Laboratory (ASL)/USGS. New China Digital Seismograph Network, 1992. doi: 10.7914/SN/IC.

Albuquerque Seismological Laboratory (ASL)/USGS. Global Telemetered Seismograph Network (USAF/USGS), 1993. doi: 10.7914/SN/GT.

Ambraseys, N. and Melville, C. *A History of Persian Earthquakes*. Cambridge Earth Science Series. Cambridge University Press, 2005. https://books.google.de/books?id=1JkfKub5vakC.

Ammon, C. J., Kanamori, H., and Lay, T. A great earthquake doublet and seismic stress transfer cycle in the central Kuril islands. *Nature*, 451(7178):561–565, 2008. doi: 10.1038/nature06521.

Ansari, S. Co-seismic stress transfer and magnitude-frequency distribution due to the 2012 Varzaqan-Ahar earthquake doublets (Mw 6.5 and 6.4), NW Iran. *Journal of Asian Earth Sciences*, 132: 129–137, 2016. doi: 10.1016/j.jseaes.2016.10.006.

Asayesh, B. M., Zarei, S., and Zafarani, H. Effects of imparted Coulomb stress changes in the seismicity and cluster of the December 2017 Hojedk (SE Iran) triplet. *International Journal of Earth Sciences*, 109:2307–2323, 2020. doi: 10.1007/s00531-020-01901-0.

Asayesh, B. M., Zafarani, H., Hainzl, S., and Sharma, S. Effects of large aftershocks on spatial aftershock forecasts during the 2017–2019 western Iran sequence. *Geophysical Journal International*, 232(1):147–161, 2022. doi: 10.1093/gji/ggac333.

Astiz, L., Lay, T., and Kanamori, H. Large intermediate-depth earthquakes and the subduction process. *Physics of the Earth and Planetary Interiors*, 53(1-2):80–166, 1988. doi: 10.1016/0031-9201(88)90138-0.

Baker, C., Jackson, J., and Priestley, K. Earthquakes on the Kazerun Line in the Zagros Mountains of Iran: strike-slip faulting within a fold-and-thrust belt. *Geophysical Journal International*, 115(1):41–61, 1993. doi: 10.1111/j.1365-246X.1993.tb05587.x.

Barnhart, W. D., Lohman, R. B., and Mellors, R. J. Active accommodation of plate convergence in Southern Iran: Earthquake locations, triggered aseismic slip, and regional strain rates. *Journal of Geophysical Research: Solid Earth*, 118(10):5699–5711, 2013. doi: 10.1002/jgrb.50380.

Bassin, C., Laske, G., and Masters, G. The Current Limits of Resolution for Surface Wave Tomography in North America. *Eos Trans. AGU*, 81(F897), 2000. https://cir.nii.ac.jp/crid/1573105976172569088.

Becker, J. J., Sandwell, D. T., Smith, W. H. F., Braud, J., Binder, B., Depner, J., Fabre, D., Factor, J., Ingalls, S., H Kim, S- and Ladner, R., Marks, K., Nelson, S., Pharaoh, A., Trimmer, R., Von Rosenberg, J., Wallace, G., and Weatherall, P. Global Bathymetry and Elevation Data at 30 Arc Seconds Resolution: SRTM30_PLUS. *Marine Geodesy*, 32:355–371, 2009. doi: 10.1080/01490410903297766.

Berberian, M. Master "blind" thrust faults hidden under the Zagros folds: active basement tectonics and surface morphotectonics. *Tectonophysics*, 241(3-4):193–224, 1995. doi: 10.1016/0040-1951(94)00185-C.

Braunmiller, J. and Nábělek, J. Geometry of continental normal faults: Seismological constraints. *Journal of Geophysical Research: Solid Earth*, 101(2):3045–3052, 1996. doi: 10.1029/95jb02882.

Carrillo Ponce, A., Dahm, T., Cesca, S., Tilmann, F., Babeyko, A., and Heimann, S. Bayesian multiple rupture plane inversion to assess rupture complexity: application to the 2018 Mw 7.9 Alaska earthquake. In *EGU General Assembly Conference Abstracts*, EGU General Assembly Conference Abstracts, pages EGU21–1583, Apr. 2021. doi: 10.5194/egusphere-egu21-1583.

Cesca, S., Braun, T., Maccaferri, F., Passarelli, L., Rivalta, E., and Dahm, T. Source modelling of the M5–6 Emilia-Romagna, Italy, earthquakes (2012 May 20–29). *Geophysical Journal International*, 193(3):1658–1672, 03 2013. doi: 10.1093/gji/ggt069.

Dahm, T., Heimann, S., Metz, M., and Isken, M. P. A self-similar dynamic rupture model based on the simplified wave-rupture analogy. *Geophysical Journal International*, 225:1586–1604, 2021. doi: 10.1093/gji/ggab045.

Dal Zilio, L. and Ampuero, J. P. Earthquake doublet in Turkey and Syria. *Commun Earth Environ*, 4:73, 2023. doi: 10.1038/s43247-023-00747-z.

Daout, S., Steinberg, A., Isken, M. P., Heimann, S., and Sudhaus, H. Illuminating the spatio-temporal evolution of the 2008–2009 qaidam earthquake sequence with the joint use of insar time series and teleseismic data. *Remote Sensing*, 12(17):1–23, 2020. doi: 10.3390/rs12172850.

Doin, M.-P., Lasserre, C., Peltzer, G., Cavalie, O., and Doubre, C. Corrections of stratified tropospheric delays in SAR interferometry: Validation with global atmospheric models. *Remote Sensing of Environment*, 160:155–170, 2015. doi: 10.1016/j.jappgeo.2009.03.010.

Donner, S., Ghods, A., Krüger, F., Rößler, D., Landgraf, A., and Ballato, P. The Ahar-Varzeghan earthquake doublet (Mw 6.4 and 6.2) of 11 August 2012: Regional seismic moment tensors and a seismotectonic interpretation. *Bulletin of the Seismological Society of America*, 105(2):791–807, 2015. doi: 10.1785/0120140042.

Dziewoński, A. M., Chou, T.-A., and Woodhouse, J. H. Determination of earthquake source parameters from waveform data for studies of global and regional seismicity. *Journal of Geophysical Research*, 86(B4):2825–2852, 1981. doi: 10.1029/JB086iB04p02825.

Edey, A., Allen, M. B., and Nilfouroushan, F. Kinematic Variation Within the Fars Arc, Eastern Zagros, and the Development of Fold-and-Thrust Belt Curvature. *Tectonics*, 39, 2020. doi: 10.1029/2019TC005941.

Ekström, G., Nettles, M., and Dziewoński, A. M. The global CMT project 2004-2010: Centroid-moment tensors for 13,017 earthquakes. *Physics of the Earth and Planetary Interiors*, 200-201: 1–9, 2012. doi: 10.1016/j.pepi.2012.04.002.

Elliott, J., Bergman, E., Copley, A., Ghods, A., Nissen, E., Oveisi, B., Tatar, M., Walters, R., and Yamini-Fard, F. The 2013 Mw 6.2 Khaki-Shonbe (Iran) Earthquake: Insights into seismic and aseismic shortening of the Zagros sedimentary cover. *Earth and Space Science*, 2(11):435–471, 2015. doi: 10.1002/2015EA000098.

Falcon, N. L. Southern Iran: Zagros Mountains. *Geological Society, London, Special Publications*, 4(1):199–211, 1974. doi: 10.1144/GSL.SP.2005.004.01.11.

Fathian, A., Atzori, S., Nazari, H., Reicherter, K., Salvi, S., Svigkas, N., Tatar, M., Tolomei, C., and Yaminifard, F. Complex co- and postseismic faulting of the 2017–2018 seismic sequence in western Iran revealed by InSAR and seismic data. *Remote Sensing of Environment*, 253(December), 2021. doi: 10.1016/j.rse.2020.112224.

Fathian, A., Atzori, S., Svigkas, N., Tolomei, C., Shugar, D. H., and Reicherter, K. Source Characteristics of the Fin Doublet Earth-

quake of 14 November 2021 (Mw 6.2 and Mw 6.3) Utilizing InSAR Data. In *IGARSS 2022 - 2022 IEEE International Geoscience and Remote Sensing Symposium*, pages 2119–2122, 2022. doi: 10.1109/IGARSS46834.2022.9883591.

Freund, R. Rotation of strike slip faults in Sistan, southeast Iran. *The Journal of Geology*, 78(2):188–200, 1970. doi: 10.1086/627500.

GEOFON Data Centre. GEOFON Seismic Network, 1993. doi: 10.14470/TR560404.

GEUS Geological Survey of Denmark and Greenland. Danish Seismological Network, 1976. https://www.fdsn.org/networks/detail/DK/.

Ghods, A., Shabanian, E., Bergman, E., Faridi, M., Donner, S., Mortezanejad, G., and Aziz-Zanjani, A. The Varzaghan-Ahar, Iran, Earthquake Doublet (Mw 6.4, 6.2): Implications for the geodynamics of northwest Iran. *Geophysical Journal International*, 203(1):522–540, 2015. doi: 10.1093/gji/ggv306.

Guo, Z., Motagh, M., Hu, J. C., Xu, G., Haghighi, M. H., Bahroudi, A., Fathian, A., and Li, S. Depth-Varying Friction on a Ramp-Flat Fault Illuminated by 3-Year InSAR Observations Following the 2017 Mw 7.3 Sarpol-e Zahab Earthquake. *Journal of Geophysical Research: Solid Earth*, 127(12), 2022. doi: 10.1029/2022JB025148.

He, P., Ding, K., and Xu, C. The 2016 Mw 6.7 Aketao earthquake in Muji range, northern Pamir: Rupture on a strike-slip fault constrained by Sentinel-1 radar interferometry and GPS. *International Journal of Applied Earth Observation and Geoinformation*, 73:99–106, 2018. doi: https://doi.org/10.1016/j.jag.2018.06.001.

Heimann, S., Isken, M., Kühn, D., Sudhaus, H., Steinberg, A., Vasyura-Bathke, H., Daout, S., Cesca, S., and Dahm, T. Grond - A probabilistic earthquake source inversion framework, 2018. doi: 10.5880/GFZ.2.1.2018.003.

Hessami, K., Koyi, H. A., Talbot, C. J., Tabasi, H., and Shabanian, E. Progressive unconformities within an evolving foreland fold–thrust belt, Zagros Mountains. *Journal of the Geological Society*, 158(6):969–981, 2001. doi: 10.1144/0016-764901-007.

Hessami, K., Jamali, F., and Tabassi, H. Major active faults of Iran. *IIEES, Tehran*, 2003.

Hogenson, K., Kristenson, H., Kennedy, J., Johnston, A., Rine, J., Logan, T. A., Zhu, J., Williams, F., Herrmann, J., and Smale, J. Hybrid Pluggable Processing Pipeline (HyP3): A Cloud-Native Infrastructure for Generic Processing of SAR Data. In *In Proceedings of the 2016 AGU Fall Meeting, San Francisco, CA, USA, 12–16 December 2016*, 2016. https://ui.adsabs.harvard.edu/abs/2016AGUFMIN21B1740H.

Ide, S. Bayesian multiple rupture plane inversion to assess rupture complexity: application to the 2018 Mw 7.9 Alaska earthquake. In Kanamori, H., editor, *Slip inversion in Earthquake Seismology*, volume 4, pages 193–224. Elsevier, 2007. doi: 10.1016/B978-044452748-6/00068-7.

India Meteorological Department. National Seismic Network of India , 2000. https://www.fdsn.org/networks/detail/IN/.

Institut de physique du globe de Paris (IPGP) and École et Observatoire des Sciences de la Terre de Strasbourg (EOST). GEOSCOPE, French Global Network of broad band seismic stations, 1982. doi: 10.18715/GEOSCOPE.G.

Isken, M., Sudhaus, H., Heimann, S., Steinberg, A., Daout, S., and Vasyura-Bathke, H. Kite - Software for Rapid Earthquake Source Optimisation from InSAR Surface Displacement, 2017. doi: 10.5880/GFZ.2.1.2017.002.

Jahani, S., Callot, J. P., Letouzey, J., and De Lamotte, D. F. The eastern termination of the Zagros Fold-and-Thrust Belt, Iran: Structures, evolution, and relationships between salt plugs, folding, and faulting. *Tectonics*, 28(6), 2009. doi: 10.1029/2008TC002418.

Jamalreyhani, M., Pousse-Beltran, L., Büyükakpınar, P., Cesca, S., Nissen, E., Ghods, A., López-Comino, J. Á., Rezapour, M., and Najafi, M. The 2019–2020 Khalili (Iran) Earthquake Sequence—Anthropogenic Seismicity in the Zagros Simply Folded Belt? *Journal of Geophysical Research: Solid Earth*, 126(12):1–19, 2021. doi: 10.1029/2021JB022797.

Jamalreyhani, M., Rezapour, M., Cesca, S., Dahm, T., Heimann, S., Sudhaus, H., and Isken, M. P. Insight into the 2017–2019 Lurestan arc seismic sequence (Zagros, Iran); complex earthquake interaction in the basement and sediments. *Geophysical Journal International*, 230:114–130, 2022. doi: https://doi.org/10.1093/gji/ggac057.

Jamalreyhani, M., Pousse-Beltran, L., Hassanzadeh, M., Arabi, S. S., Bergman, E. A., Shamszadeh, A., Arvin, S., Fariborzi, N., and Songhori, A. Co-seismic slip of the 18 April 2021 Mw 5.9 Genaveh earthquake in the South Dezful Embayment of Zagros (Iran) and its aftershock sequence. *Seismica*, 2(1), 2023. doi: 10.26443/seismica.v2i1.246.

Jia, Z., Shen, Z., Zhan, Z., Li, C., Peng, Z., and Gurnis, M. The 2018 Fiji Mw 8.2 and 7.9 deep earthquakes: One doublet in two slabs. *Earth and Planetary Science Letters*, 531:115997, 2020. doi: https://doi.org/10.1016/j.epsl.2019.115997.

Jia, Z., Zhan, Z., and Kanamori, H. The 2021 South Sandwich Island Mw 8.2 earthquake: a slow event sandwiched between regular ruptures. *Geophys. Res. Lett.*, 49:1–8, 2022. doi: 10.1029/2021GL097104.

Jónsson, S., Zebker, H., Segall, P., and Amelung, F. Fault slip distribution of the 1999 Mw 7.1 Hector Mine, California, earthquake, estimated from satellite radar and GPS measurements. *Bulletin of the Seismological Society of America*, 92(4):1377–1389, 2002. doi: 10.1785/0120000922.

Karasözen, E., Nissen, E., Bergman, E. A., and Ghods, A. Seismotectonics of the Zagros (Iran) From Orogen-Wide, Calibrated Earthquake Relocations. *Journal of Geophysical Research: Solid Earth*, 124(8):9109–9129, 2019. doi: 10.1029/2019JB017336.

Kennett, B. L. N., Engdahl, E. R., and Buland, R. Constraints on seismic velocities in the Earth from traveltimes. *Geophysical Journal International*, 122(1):108–124, 1995. doi: 10.1111/j.1365-246X.1995.tb03540.x.

Lay, T. The surge of great earthquakes from 2004 to 2014. *Earth and Planetary Science Letters*, 409:133–146, 2015. doi: 10.1016/j.epsl.2014.10.047.

Lay, T. and Kanamori, H. Earthquake Doublets in the Solomon Islands. *Physics ofthe Earth and Planetary Interiors*, 21:283–304, 1980. doi: 10.1016/0031-9201(80)90134-X.

Lohman, R. B. and Barnhart, W. D. Evaluation of earthquake triggering during the 2005–2008 earthquake sequence on Qeshm Island, Iran. *Journal of Geophysical Research*, 115, 2010. doi: https://doi.org/10.1029/2010JB007710.

LTD Seismological Experience and Methodology Expedition of the Committee of Science of the Ministry of Education and Science of the Republic of Kazakhstan. Seismic network of the Seismological Experience and Methodology Expedition CS MES RK, 2003. doi: 10.7914/SN/QZ.

Masson, F., Chéry, J., Hatzfeld, D., Martinod, J., Vernant, P., Tavakoli, F., and Ghafory-Ashtiani, M. Seismic versus aseismic deformation in Iran inferred from earthquakes and geodetic data. *Geophysical Journal International*, 160(1):217–226, 2005. doi: 10.1111/j.1365-246X.2004.02465.x.

Metz, M. A quasi-dynamic and self-consistent rupture model to simulate earthquake ruptures. *Universität Potsdam*, 2019. doi:

10.25932/publishup-47310.

Metz, M., Vera, F., Carrillo Ponce, A., Cesca, S., Babeyko, A., Dahm, T., Saul, J., and Tilmann, F. Seismic and Tsunamigenic Characteristics of a Multimodal Rupture of Rapid and Slow Stages: The Example of the Complex 12 August 2021 South Sandwich Earthquake. *Journal of Geophysical Research: Solid Earth*, 127(11), 2022. doi: 10.1029/2022jb024646.

Momeni, S. and Tatar, M. Mainshocks/aftershocks study of the August 2012 earthquake doublet on Ahar-Varzaghan complex fault system (NW Iran). *Physics of the Earth and Planetary Interiors*, 283:67–81, 2018. doi: https://-doi.org/10.1016/j.pepi.2018.08.001.

Nemati, M. The November 2021 Fin (SE Zagros , Iran) doublet earthquakes of reverse faults in a transpressional tectonic regime. Technical report, Shahid Bahonar University of Kerman, 2022. https://doi.org/10.21203/rs.3.rs-1314781/v1.

Ni, J. and Barazangi, M. Seismotectonics of the Zagros continental collision zone and a comparison with the Himalayas. *Journal of Geophysical Research: Solid Earth*, 91(B8):8205–8218, 1986. doi: 10.1029/JB091iB08p08205.

Nissen, E., Ghorashi, M., Jackson, J., Parsons, B., and Talebian, M. The 2005 Qeshm Island earthquake (Iran) - A link between buried reverse faulting and surface folding in the Zagros Simply Folded Belt? *Geophysical Journal International*, 171(1):326–338, 2007. doi: 10.1111/j.1365-246X.2007.03514.x.

Nissen, E., Yamini-Fard, F., Tatar, M., Gholamzadeh, A., Bergman, E., Elliott, J. R., Jackson, J. A., and Parsons, B. The vertical separation of mainshock rupture and microseismicity at Qeshm island in the Zagros fold-and-thrust belt, Iran. *Earth and Planetary Science Letters*, 296(3-4):181–194, 2010. doi: 10.1016/j.epsl.2010.04.049.

Nissen, E., Tatar, M., Jackson, J. A., and Allen, M. B. New views on earthquake faulting in the Zagros fold-and-thrust belt of Iran. *Geophysical Journal International*, 186(3):928–944, 2011. doi: 10.1111/j.1365-246X.2011.05119.x.

Nissen, E., Jackson, J., Jahani, S., and Tatar, M. Zagros "phantom earthquakes" reassessed - The interplay of seismicity and deep salt flow in the Simply Folded Belt? *Journal of Geophysical Research: Solid Earth*, 119(4):3561–3583, 2014. doi: 10.1002/2013JB010796.

Nissen, E., Ghods, A., Karasözen, E., Elliott, J. R., Barnhart, W. D., Bergman, E. A., Hayes, G. P., Jamal-Reyhani, M., Nemati, M., Tan, F., Abdulnaby, W., Benz, H. M., Shahvar, M. P., Talebian, M., and Chen, L. The 12 November 2017 M w 7.3 Ezgeleh-Sarpolzahab (Iran) Earthquake and Active Tectonics of the Lurestan Arc. *Journal of Geophysical Research: Solid Earth*, 124(2):2124–2152, 2019. doi: 10.1029/2018JB016221.

Okada, Y. Gravity and potential changes due to shear and tensile faults in a half-space. *Journal of Geophysical Research*, 82(2): 1018–1040, 1992. doi: 10.1029/92JB00178.

Oveisi, B., Lavé, J., Van Der Beek, P., Carcaillet, J., Benedetti, L., and Aubourg, C. Thick-and thin-skinned deformation rates in the central Zagros simple folded zone (Iran) indicated by displacement of geomorphic surfaces. *Geophysical Journal International*, 176(2):627–654, 2009. doi: 10.1111/j.1365-246X.2008.04002.x.

Quinteros, J., Strollo, A., Evans, P. L., Hanka, W., Heinloo, A., Hemmleb, S., Hillmann, L., Jaeckel, K., Kind, R., Saul, J., Zieke, T., and Tilmann, F. The GEOFON Program in 2020. *Seismological Research Letters*, 92(3):1610–1622, 02 2021. doi: 10.1785/0220200415.

Regard, V., Bellier, O., Thomas, J.-C., Abbassi, M., Mercier, J., Shabanian, E., Feghhi, K., and Soleymani, S. Accommodation of Arabia-Eurasia convergence in the Zagros-Makran transfer zone, SE Iran: A transition between collision and subduction through a young deforming system. *Tectonics*, 23(4), 2004. doi: 10.1029/2003TC001599.

Regional Integrated Multi-Hazard Early Warning System (RIMES Thailand). Regional Integrated Multi-Hazard Early Warning System, 2008. doi: 10.7914/SN/RM.

Rezapour, M. and Jamalreyhani, M. R. Source fault analyses from InSAR data and aftershocks for the Fin doublet earthquakes on 14 November 2021 in Hormozgan province, South Iran. *Earth and Space Physics*, 2022. doi: 10.22059/jesphys.2022.337959.1007399.

Roustaei, M., Nissen, E., Abbassi, M., Gholamzadeh, A., Ghorashi, M., Tatar, M., Yamini-Fard, F., Bergman, E., Jackson, J., and Parsons, B. The 2006 March 25 Fin earthquakes (Iran) - insights into the vertical extents of faulting in the Zagros Simply Folded Belt. *Geophysical Journal International*, 181(3):1275–1291, 2010. doi: 10.1111/j.1365-246X.2010.04601.x.

San Fernando Royal Naval Observatory (ROA), Universidad Complutense De Madrid (UCM), Helmholtz-Zentrum Potsdam Deutsches GeoForschungsZentrum (GFZ), Universidade De Évora (UEVORA, Portugal) and Institute Scientifique Of Rabat (ISRABAT, Morocco). The Western Mediterranean BB seismic Network, 1996. doi: 10.14470/JZ581150.

Savidge, E., Nissen, E., Nemati, M., Karasözen, E., Hollingsworth, J., Talebian, M., Bergman, E., Ghods, A., Ghorashi, M., Kosari, E., et al. The December 2017 Hojedk (Iran) earthquake triplet—sequential rupture of shallow reverse faults in a strike-slip restraining bend. *Geophysical Journal International*, 217(2): 909–925, 2019. doi: 10.1093/gji/ggz053.

Scripps Institution of Oceanography. Global Seismograph Network - IRIS/IDA, 1986. doi: 10.7914/SN/II.

Sokos, E., Kiratzi, A., Gallovič, F., Zahradník, J., Serpetsidaki, A., Plicka, V., Janský, J., Kostelecký, J., and Tselentis, G. A. Rupture process of the 2014 Cephalonia, Greece, earthquake doublet (Mw6) as inferred from regional and local seismic data. *Tectonophysics*, 656:131–141, 2015. doi: 10.1016/j.tecto.2015.06.013.

Steinberg, A., Sudhaus, H., Heimann, S., and Krüger, F. Sensitivity of InSAR and teleseismic observations to earthquake rupture segmentation. *Geophysical Journal International*, 223(2): 875–907, 2020. doi: 10.1093/gji/ggaa351.

Steinberg, A., Sudhaus, H., and Krüger, F. Using teleseismic backprojection and InSAR to obtain segmentation information for large earthquakes: a case study of the 2016 Mw 6.6 Muji earthquake. *Geophysical Journal International*, 2022. doi: 10.1093/gji/ggac392.

Stoecklin, J. Structural history and tectonics of Iran: a review. *AAPG bulletin*, 52(7):1229–1258, 1968. doi: 10.1306/5D25C4A5-16C1-11D7-8645000102C1865D.

Sudhaus, H. and Jónsson, S. Improved source modelling through combined use of InSAR and GPS under consideration of correlated data errors: Application to the June 2000 Kleifarvatn earthquake, Iceland. *Geophysical Journal International*, 176(2): 389–404, 2009. doi: 10.1111/j.1365-246X.2008.03989.x.

Talebian, M. and Jackson, J. A reappraisal of earthquake focal mechanisms and active shortening in the Zagros mountains of Iran. *Geophysical Journal International*, 156(3):506–526, 2004. doi: 10.1111/j.1365-246X.2004.02092.x.

Tatar, M., Hatzfeld, D., and Ghafory-Ashtiany, M. Tectonics of the Central Zagros (Iran) deduced from microearthquake seismicity. *Geophysical Journal International*, 156(2):255–266, 2004. doi: 10.1111/j.1365-246X.2003.02145.x.

Taymaz, T., Ganas, A., Berberian, M., Eken, T., Irmak, T. S., Kapetanidis, V., Yolsal-Çevikbilen, S., Erman, C., Keleş, D., Esmaeili, C., Tsironi, V., and Özkan, B. The 23 February 2020 Qotur-Ravian

earthquake doublet at the Iranian-Turkish border: Seismological and InSAR evidence for escape tectonics. *Tectonophysics*, 838:229482, 2022. doi: 10.1016/j.tecto.2022.229482.

Thapa, D. R., Tao, X., Fan, F., and Tao, Z. Aftershock analysis of the 2015 Gorkha-Dolakha (Central Nepal) earthquake doublet. *Heliyon*, 4(7):e00678, 2018. doi: 10.1016/j.heliyon.2018.e00678.

Trugman, D. T. and Shearer, P. M. GrowClust: A Hierarchical clustering algorithm for relative earthquake relocation, with application to the Spanish Springs and Sheldon, Nevada, earthquake sequences. *Seismological Research Letters*, 88(2):379–391, 2017. doi: 10.1785/0220160188.

Trugman, D. T., Chamberlain, C. J., Savvaidis, A., and Lomax, A. GrowClust3D.jl: A Julia Package for the Relative Relocation of Earthquake Hypocenters Using 3D Velocity Models. *Seismological Research Letters*, 94(1):443–456, 2023. doi: 10.1785/0220220193.

Vernant, P., Nilforoushan, F., Hatzfeld, D., Abbassi, M., Vigny, C., Masson, F., Nankali, H., Martinod, J., Ashtiani, A., Bayer, R., et al. Present-day crustal deformation and plate kinematics in the Middle East constrained by GPS measurements in Iran and northern Oman. *Geophysical Journal International*, 157(1): 381–398, 2004. doi: 10.1111/j.1365-246X.2004.02222.x.

Walker, R. and Jackson, J. Offset and evolution of the Gowk fault, SE Iran: a major intra-continental strike-slip system. *Journal of structural Geology*, 24(11):1677–1698, 2002. doi: 10.1016/S0191-8141(01)00170-5.

Walker, R. T., Andalibi, M. J., Gheitanchi, M. R., Jackson, J. A., Karegar, S., and Priestley, K. Seismological and field observations from the 1990 November 6 Furg (Hormozgan) earthquake: A rare case of surface rupture in the Zagros mountains of Iran. *Geophysical Journal International*, 163(2):567–579, 2005. doi: 10.1111/j.1365-246X.2005.02731.x.

Wang, R. A simple orthonormalization method for stable and efficient computation of Green's functions. *Bulletin of the Seismological Society of America*, 89:733–741, 1999. doi: 10.1785/BSSA0890030733.

Wang, R. The dislocation theory: a consistent way for including the gravity effect in (visco)elastic plane-earth models. *Geophysical Journal International*, 161:191–196, 2005. doi: 10.1111/j.1365-246X.2005.02614.x.

Wang, R., Lorenzo-Martín, F., and Roth, F. Computation of deformation induced by earthquakes in a multi-layered elastic crust - FORTRAN programs EDGRN/EDCMP. *Computer and Geosciences*, 29:195–207, 2003. doi: 10.1016/S0098-3004(02)00111-5.

Wang, R., Lorenzo-Martín, F., and Roth, F. PSGRN/PSCMP - a new code for calculating co- and post-seismic deformation, geoid and gravity changes based on the viscoelastic-gravitational dislocation theory. *Computer and Geosciences*, 32:527–541, 2006. doi: 10.1016/j.cageo.2005.08.006.

Wessel, P. and Smith, W. H. F. A global, self-consistent, hierarchical, high-resolution shoreline database. *Journal of Geophysical Research*, 101:8741–8743, 1996. doi: 10.1029/96JB00104.

Wessel, P., Smith, W. H., Scharroo, R., Luis, J., and Wobbe, F. Generic mapping tools: Improved version released. *Eos*, 94(45): 409–410, 2013. doi: 10.1002/2013EO450001.

Weston, J., Ferreira, A. M., and Funning, G. J. Systematic comparisons of earthquake source models determined using InSAR and seismic data. *Tectonophysics*, 532-535:61–81, 2012. doi: 10.1016/j.tecto.2012.02.001.

Xu, Z. and Schwartz, S. Y. Large earthquake doublets and fault plane heterogeneity in the northern Solomon Islands subduction zone. *Pure and Applied Geophysics PAGEOPH*, 140(2): 365–390, 1993. doi: 10.1007/BF00879412.

Yamini-Fard, F., Hatzfeld, D., Farahbod, A., Paul, A., and Mokhtari, M. The diffuse transition between the Zagros continental collision and the Makran oceanic subduction (Iran): microearthquake seismicity and crustal structure. *Geophysical Journal International*, 170(1):182–194, 2007. doi: 10.1111/j.1365-246X.2006.03232.x.

Yaminifard, F., Tatar, M., Hessami, K., Gholamzadeh, A., and Bergman, E. Aftershock analysis of the 2005 November 27 (Mw 5.8) Qeshm Island earthquake (Zagros-Iran): Triggering of strike-slip faults at the basement. *Journal of Geodynamics*, 61: 138–147, 2012. doi: 10.1016/j.jog.2012.04.005.

Yang, Y.-h., Li, X., Hu, J.-c., Song, J., Zhao, J., and Yassaghi, A. The 2022 Hormozgan Doublet Earthquake : Two Blind Thrusts-Related Folding in Zagros Fold-And-Thrust Belt , Southeast Iran. *Geophysical Research Letters*, 50, 2023. doi: 10.1029/2022GL101902.

Ye, L., Lay, T., Kanamori, H., and Koper, K. D. Energy Release of the 2013 Mw 8.3 Sea of Okhotsk Earthquake and Deep Slab Stress Heterogeneity. *Science*, 341(September):1380–1384, 2013. doi: 10.1126/science.1242032.

Ye, L., Lay, T., Kanamori, H., Zhan, Z., and Duputel, Z. Diverse rupture processes in the 2015 Peru deep earthquake doublet. *Science Advances*, 2(6):1989–1990, 2016. doi: 10.1126/sciadv.1600581.

Yu, C., Penna, N. T., and Li, Z. Generation of real-time mode high-resolution water vapor fields from GPS observations. *Journal of Geophysical Research: Atmospheres*, 122:2008–2025, 2017. doi: 10.1002/2016JD025753.

Yu, C., Li, Z., and Penna, N. T. Interferometric synthetic aperture radar atmospheric correction using a GPS-based iterative tropospheric decomposition model. *Remote Sensing of Environment*, 204:109–121, 2018a. doi: 10.1016/j.rse.2017.10.038.

Yu, C., Li, Z., Penna, N. T., and Crippa, P. Generic Atmospheric Correction Model for Interferometric Synthetic Aperture Radar Observations. *Journal of Geophysical Research: Solid Earth*, 123: 9202–9222, 2018b. doi: 10.1029/2017JB015305.

Yunjun, Z., Fattahi, H., and Amelung, F. Small baseline InSAR time series analysis: Unwrapping error correction and noise reduction. *Remote Sens.*, 14(336), 2022. doi: 10.1016/j.cageo.2019.104331.

Zhang, X., Feng, W., Li, D., Yin, F., and Yi, L. Diverse rupture processes of the 2014 Kangding, China, earthquake doublet (MW 6.0 and 5.7) and driving mechanisms of aftershocks. *Tectonophysics*, 820:229118, 2021. doi: 10.1016/j.tecto.2021.229118.

Zhao, X., Xu, C., Wen, Y., He, K., and Yang, J. Early post-seismic deformation of the 2017 Mw 7.3 Darbandikhan, Iran/Iraq Earthquake on a flat-ramp-flat fault. *Tectonophysics*, 853:229809, 2023. doi: 10.1016/j.tecto.2023.229809.